Karlsruhe Institute of Technology

Ignition in Thin Confined Spaces

Bachelor Thesis of

Mohammad Mahdi Malayeri

Karlsruhe Institute of Technology (KIT)
Institute of Technical Thermodynamics (ITT)
durch Mittel der Dr.Ing. Willy-Höfler-Stiftung gefördert

Advisor at KIT:	Prof. Dr. rer. nat. habil. Ulrich Maas
Advisor at Caltech:	Prof. Joseph E. Shepherd
Co-Advisor at Caltech:	Mr. Branson Davis

09.09.2024 – 09.12.2024

Karlsruher Institut für Technologie
Fakultät für Maschinebau
Intitut für Technische Thermodynamik (ITT)
KIT Campus Süd
Engelbert-Arnold-Str. 4
76131 Karlsruhe

I hereby assure truthfully that I have independently authored the thesis, fully and accurately referenced all used resources, and clearly indicated everything that has been taken unchanged or with modifications from the work of others. Furthermore, I confirm compliance with the Karlsruhe Institute of Technology (KIT) regulations for ensuring good scientific practice in their respective valid version.

Karlsruhe, 09.12.2024

. . . . . .

(Mohammad Mahdi Malayeri)

Acknowledgements

First and foremost, I would like to express my heartfelt gratitude to my advisors, Professor Ulrich Maas and Professor Joseph E. Shepherd, for their invaluable guidance and for enabling my research stay at the California Institute of Technology (Caltech). Professor Maas inspired my initial fascination with thermodynamics through his engaging lectures at the Karlsruhe Institute of Technology (KIT), which laid the foundation for my academic journey in this field. Professor Shepherd has significantly deepened my interest in research and the topic of ignition through his enthusiasm and exceptional supervision. I am deeply appreciative of the opportunity to work in the stimulating and highly esteemed scientific environment of the Explosion Dynamics Laboratory at Caltech.

I would also like to extend my sincere thanks to Mr. Branson Davis of the Explosion Dynamics Laboratory for his continuous support and insightful advice throughout my research stay in the United States.

My research stay was generously funded by the Dr. Ing. Willy-Höfler-Foundation which is coordinated by the faculty of Mechanical Engineering at KIT. Without this financial support, it would not have been possible for me to pursue this invaluable research experience. In this respect, in particular, I am grateful to the Mechanical Engineering Department at KIT, and particularly to Professor Maas, for his efforts in helping me secure this scholarship.

Lastly, I would like to express my deepest appreciation to my parents, whose unwavering financial and emotional support carried me through the challenging times of my thesis. Their encouragement has been a pillar of strength throughout this journey.

Abstract

Hot surface ignition is relevant in the context of aviation safety. The critical conditions leading to thermal ignition are generally highly dependent on the geometrical configuration. This study numerically investigates the ignition behavior in Hele-Shaw cells. Initially, it has mathematically and numerically been shown that the velocity profile over the narrow gap is parabolic within the boundary conditions considered in this study. After that, the implemented equations in OpenFOAM, an open-source computational fluid dynamics software, were averaged over the gap, and then a new solver was built. This, in turn, reduced the problem into two dimensions. Next, the fluid dynamics in Hele-Shaw cells with air and various lengths and heights were examined. It was observed that circulation occurs within the cells due to heat transfer convection. The fluid near the hot wall rises, then moves toward the cold wall, descends along it, and is subsequently drawn back toward the hot wall, completing the circulation cycle. The thermal boundary layers close to the hot wall were narrow, which means that the heat loss in this area was high compared to the rest of the domain where the thermal boundary layers were broad. After investigating the flow fields of the Hele-Shaw cells, the simulations with a mixture of air and n-hexane with an one-step irreversible chemistry model were conducted using the initial conditions from simulations performed with only air. The zero-dimensional adiabatic reaction ignition delay time was 0.335 s, which is the zero-dimensional adiabatic reaction limit. For Hele-Shaw cells with a constant length of 0.1 m, and a gap of 0.005 m, it was observed that the subcritical limit has to be between a height of 0.045 m and 0.050 m. It was also inferred that the aspect ratio (length divided by height) was not an appropriate non-dimensional parameter to compare the different Hele-Shaw cells. Instead, the surface area (length multiplied by height) was a better metric to compare different Hele-Shaw cells. The results also confirmed that as the surface area increased, lower ignition delay time should be expected. Finally, the results of this provided insights into the thermal and chemical dynamics in confined geometries, contributing to an improved understanding of ignition mechanisms in Hele-Shaw cells and their implications for the aviation safety.

Zusammenfassung

Zündung durch heiße Oberflächen ist wichtig im Kontext der Luftfahrtsicherheit. Die kritischen Bedingungen, die zu einer thermischen Zündung führen, hängen in der Regel stark von der geometrischen Konfiguration ab. In dieser Arbeit wird das Zündverhalten in Hele-Shaw-Zellen numerisch untersucht.

Zu Beginn wurde mathematisch und numerisch gezeigt, dass das Geschwindigkeitsprofil über den schmalen Spalt unter den in dieser Studie berücksichtigten Randbedingungen parabolisch ist. Anschließend wurden die in OpenFOAM, einer Open-Source-Software für numerische Strömungsmechanik, implementierten Gleichungen über den Spalt gemittelt, und ein neuer Solver wurde entwickelt. Dadurch wurde das Problem auf zwei Dimensionen reduziert.

Im nächsten Schritt wurden die Strömungsdynamik in Hele-Shaw-Zellen mit Luft sowie verschiedene Längen und Höhen der Zellen untersucht. Es wurde beobachtet, dass aufgrund der Wärmeübertragung durch Konvektion eine Zirkulation innerhalb der Zellen entsteht. Die Strömung in der Nähe der heißen Wand steigt auf, bewegt sich dann in Richtung der kalten Wand, sinkt dort ab und wird anschließend wieder in Richtung der heißen Wand zurückgeführt, wodurch der Zirkulationszyklus abgeschlossen wird.

Die thermischen Grenzschichten in der Nähe der heißen Wand waren schmal, was bedeutet, dass der Wärmeverlust in diesem Bereich höher war als im restlichen Bereich der Zelle, wo die thermischen Grenzschichten breiter waren. Nachdem die Strömungsfelder der Hele-Shaw-Zellen analysiert worden waren, wurden Simulationen mit einem Gemisch aus Luft und n-Hexan sowie einem einstufigen irreversiblen Reaktionsmodell durchgeführt, wobei die Anfangsbedingungen aus den Simulation Ergebnissen mit reiner Luft übernommen wurden.

Die adiabatische Zündverzugszeit im null-dimensionalen Modell betrug 0,335 s, was der Grenze der null-dimensionalen adiabatischen Reaktion entspricht. Für Hele-Shaw-Zellen mit einer konstanten Länge von 0,1 m und einem Spalt von 0,005 m wurde festgestellt, dass die subkritische Grenze zwischen einer Höhe von 0,045 m und 0,050 m liegen muss. Es wurde außerdem festgestellt, dass das Seitenverhältnis (Länge geteilt durch Höhe) kein geeigneter dimensionsloser Parameter ist, um verschiedene Hele-Shaw-Zellen zu vergleichen. Stattdessen erwies sich die Oberfläche (Länge multipliziert mit Höhe) als besseres Maß für den Vergleich verschiedener Hele-Shaw-Zellen.

Die Ergebnisse bestätigten auch, dass mit zunehmender Oberfläche eine geringere Zündverzugszeit zu erwarten ist. Schließlich lieferte die Studie Einblicke in die thermischen und chemischen Dynamiken in begrenzten Geometrien und trug zu einem verbesserten Verständnis der Zündmechanismen in Hele-Shaw-Zellen sowie deren Bedeutung für die Luftfahrtsicherheit bei.

Contents

Acknowledgements i

Abstract iii

Zusammenfassung v

1 Introduction 1
- 1.1 Natural Convection in Hele-Shaw Cells . . . 1
- 1.2 Thermal Ignition . . . 2
- 1.3 Research Objectives . . . 3
- 1.4 Scope of present work . . . 3

2 Fundamentals 5
- 2.1 Non-Boussinesq Natural Convection . . . 5
  - 2.1.1 Boussinesq Approximation . . . 5
- 2.2 Parabolic Velocity Shape Across the Gap . . . 6
- 2.3 Governing Equations . . . 8

3 Problem Statement 9
- 3.1 Assumptions and Simplifications . . . 10

4 Numerical Setup and Methodologies for Fluid Dynamics 11
- 4.1 Transport Model . . . 11
- 4.2 Thermodynamic Property Characteristics . . . 12
- 4.3 Mesh Sensitivity Study . . . 13
  - 4.3.1 Number of Cells . . . 15
  - 4.3.2 Expansion Ratio . . . 16

5 Numerical Setup and Methodology for Ignition Dynamics 21
- 5.1 1D Comparison of the `ReactingHeleShawFoam` Solver . . . 22
- 5.2 Zero-Dimensional Adiabatic Ignition Delay Time . . . 24

6 Results and Discussion 27
- 6.1 Validation of the Developed Solver . . . 27
  - 6.1.1 Parabolic Velocity Profile Over the Gap . . . 27
  - 6.1.2 Temperature Profile Over the Gap . . . 28
  - 6.1.3 Comparison of Two Solvers . . . 31
- 6.2 Fluid Dynamics . . . 33
- 6.3 Ignition Dynamics . . . 40

7 Conclusions **45**
7.1 Future Work 46

Bibliography **47**

List of Figures

1.1 Qualitative progression of the Nusselt number (Nu_L) depending on the Rayleigh number (Ra_L) for vertical confined spaces, translated from [29] 2
1.2 Methodology flowchart of the present study 4

2.1 Parabolic velocity profile over the gap 6

3.1 Diagram of the Hele-Shaw Cell 9

4.1 Comparison of the Sutherland law to the calculated viscosity by Canetra with $A_s = 1.4792e-6\ K^{-0.5}s^{-1}m^{-1}kg$ and $T_s = 116$ K 12
4.2 Thermodynamic properties based on the JANAF model 14
4.3 Optimal computational domain for a Hele-Shaw cell with dimensions of 0.1 m in both height and length and a gap size of 0.005 m with cell compression near the walls 15
4.4 Global mesh sensitivity with a uniform grid 16
4.5 Local Mesh Sensitivity Analysis 17
4.6 Mesh grading along a block edge 17
4.7 Global mesh sensitivity analysis with varying expansion ratios 18
4.8 Local Mesh Sensitivity Analysis with varying expansion ratio in the x-direction, and with an expansion ratio in the y-direction of 1 18
4.9 Local Mesh Sensitivity Analysis with varying expansion ratio in the y-direction, and with an expansion ratio in the x-direction of 20 19

5.1 Lewis number of hexane in hexane-air mixtures as a function of hexane mole fraction 22
5.2 Optimal computational domain for a Hele-Shaw cell with dimensions of 0.1 m in both height and length and a gap size of 0.005 m with cell compression near the walls, and a cell size of 167 μm in top-left quarter of the domain 23
5.3 Comparison of the `ReactingHeleShawFoam` solver (solid colored lines) to the `buoyantReactingFoam` solver (black dashed lines) for a hot wall temperature of 1000 K, and a cold wall temperature of 300 K 24
5.4 Comparison of the `ReactingHeleShawFoam` solver with the one-step reaction (dashed lines) to a high fidelity multi-species reaction simulation (solid lines) for a hot wall temperature of 1000 K, and a cold wall temperature of 300 K 25
5.5 Zero-dimensional adiabatic reaction of a stoichiometric air and n-hexane mixture to define the ignition delay time 25

6.1 Parabolic functions fitted to the velocity profiles across the gap of a Hele-Shaw cell with a length of 0.1 m, a height of 0.3 m, and a gap width of 0.005 m after reaching the steady-state solution 29
6.2 Velocity profile over the line in the z-direction passing through $\underline{x}_D = (0.005, 0.005)$ m of a Hele-Shaw cell with a length of 0.1 m, a height of 0.3 m, and a gap width of 0.005 m after reaching the steady-state solution 30
6.3 Temperature profiles across the gap of a Hele-Shaw cell with a length of 0.1m, a height of 0.3m, and a gap width of 0.005 m after reaching the steady-state solution 30
6.4 Comparison of the `buoyantPimpleFoam` solver (3-D, no approximations) to the `Adiabatic_heleShawFoam` solver (with Hele-Shaw approximations) of a Hele-Shaw cell with a length of 0.1m, a height of 0.3m, and a gap width of 0.005 m after reaching the steady-state solution 32
6.5 Steady-state simulation results for a Hele-Shaw cell with a length and height of 0.1 m 34
6.6 Steady-state simulation results for Hele-Shaw cells with a length of 0.1 m and 0.3 m, and a height of 0.3 m and 0.1 m 35
6.7 Temperature profile over horizontal lines of the steady simulation for the Hele-Shaw cell with a length of 0.1 m and a height of 0.3 m 36
6.8 Velocity component in the x-direction profile over horizontal lines of the steady simulation for the Hele-Shaw cell with a length of 0.1 m and a height of 0.3 m 36
6.9 Velocity component in the y-direction profile over horizontal lines of the steady simulation for the Hele-Shaw cell with a length of 0.1 m and a height of 0.3 m 37
6.10 Velocity component in the x-direction profile over horizontal lines of the steady simulation for the Hele-Shaw cell with a length of 0.3 m and a height of 0.1 m 37
6.11 Velocity component in the x-direction profile over horizontal lines of the steady simulation for the Hele-Shaw cell with a length of 0.1 m and a height of 0.3 m 38
6.12 Velocity component in the y-direction profile over horizontal lines of the steady simulation for the Hele-Shaw cell with a length of 0.3 m and a height of 0.1 m 38
6.13 Steady-state simulation results for a Hele-Shaw cell with a length of 0.1 m and a height of 1.0 m. The right vertical axis represents the temperature, while the left vertical axis represents the velocity components. 39
6.14 Steady-state simulation results for a Hele-Shaw cell with a length of 1.0 m and a height of 0.1 m. The right vertical axis represents the temperature, while the left vertical axis represents the velocity components. 40
6.15 Ignition kernel and the initial flame propagation of a Hele-Shaw cell with a length and height of 0.1 m 41
6.16 Ignition delay times as a function of the varying height of the Hele-Shaw cell with constant lengths of 0.1 m 42

6.17 Ignition delay times as a function of the varying length of the Hele_Shaw cell with constant heights of 0.1 m 43
6.18 Steady-state simulation results for a Hele-Shaw cell with a length of 0.1 m and a height of 1.0 m. The right vertical axis represents the temperature, while the left vertical axis represents the velocity components. 43

List of Tables

4.1 Coefficients for the transport model in OpenFOAM 12
4.2 JANAF high-temperature coefficients 13
4.3 JANAF low-temperature coefficients 14

5.1 Constants to model a one-step irreversible stoichiometric air and n-hexane mixture at a pressure of one bar and a temperature of 300 K 23

6.1 SSE values for different points to demonstrate the goodness of fit 28
6.2 Values to quantities the global comparison of the `buoyantPimpleFoam` and `Adiabatic_heleShawFoam` solver 33
6.3 Calculated values to determine the Rayleigh number of air at 600 K . . . 33
6.4 Simulated cases without chemistry with the `Adiabatic_heleShawFoam` solver for air 33

1 Introduction

Accidental thermal ignition may potentially cause profound hazards to the aviation industry [6]. It can cause severe structural damage, economic loss, and death. Elimination or mitigation of its occurrence is key to the safe operation of flammable systems. Such ignition events can arise from numerous sources including, but not limited to, open flames as well as hot particles and jets. In aircraft in particular, compartments within and around fuel tanks, engines, and auxiliary power units are inevitably subject to ignition hazards due to their hot surfaces near combustible substances. The presence of hot surfaces is unavoidable in aircraft. As a result, an in-depth understanding of this event would facilitate the prevention of accidental combustion in aircraft. The Boeing 747-131 Trans World Airlines 800 flight in 1996 from New York to Paris is a tragic example of the importance of ignition hazards [32]. The aircraft broke up in flight at an altitude of 13,800 feet, possibly due to hot surface ignition and explosion that occurred in the center wing tank [9].

1.1 Natural Convection in Hele-Shaw Cells

Heat transfer is energy in transit due to a temperature difference [4]. There are three modes of heat transfer: conduction, convection, and radiation. Natural or free convection in a gas layer occurs when a density difference drives a buoyancy force. Free convection across a closed cavity between vertical boundaries, in which one dimension is small compared to the two other dimensions (Hele-Shaw cell) began initially by Batchelor in 1954 [3]. He was interested in measuring the heat transfer in double-pane windows of varying sizes.

Usually, studies on natural convection between two plates are done in a way that one of the dimensions is assumed to be infinitely long, and therefore the problem reduces to two dimensions. Elder [12, 13, 14], McGregor and Emery [24], and Catton [7] studied the configuration illustrated in Fig. 1.1 where the z-direction is assumed to be infinitely long. The Rayleigh number (Ra_L) is defined in the described figure by:

$$Ra_L = \frac{\gamma g \Delta T L^3}{\kappa \nu} \tag{1.1}$$

where $\gamma, g, \Delta T, \kappa, L$, and ν are the coefficient of cubical expansion, acceleration of gravity, the temperature difference of the cold and hot wall, thermal diffusivity, vertical dimension, and kinematic viscosity, respectively. It is worth mentioning that the described Rayleigh number in Eq. 1.1 is criticized in Refs. [18, 25].

Thermal convection in Hele-Shaw cells has been previously studied by Hartline et al. [18] with a different configuration. The Hele-Shaw cell is heated from the bottom and the walls are assumed to be isothermal. Vorontsov et al. [35] also investigated thermal

convection in a Hele-Shaw cell. In this study, one of the vertical narrow walls is heated, and the other walls either have constant wall temperature or uniform wall heat flux.

The configuration studied in the present work has a similar configuration as shown in Fig. 1.1 with the difference that the width of the configuration (length in z-direction) is small compared to the length and height, and the walls at the front and back (xy-planes) are adiabatic. Since no prior studies have investigated convection in the configuration examined in this work, this thesis aims to fill this research gap.

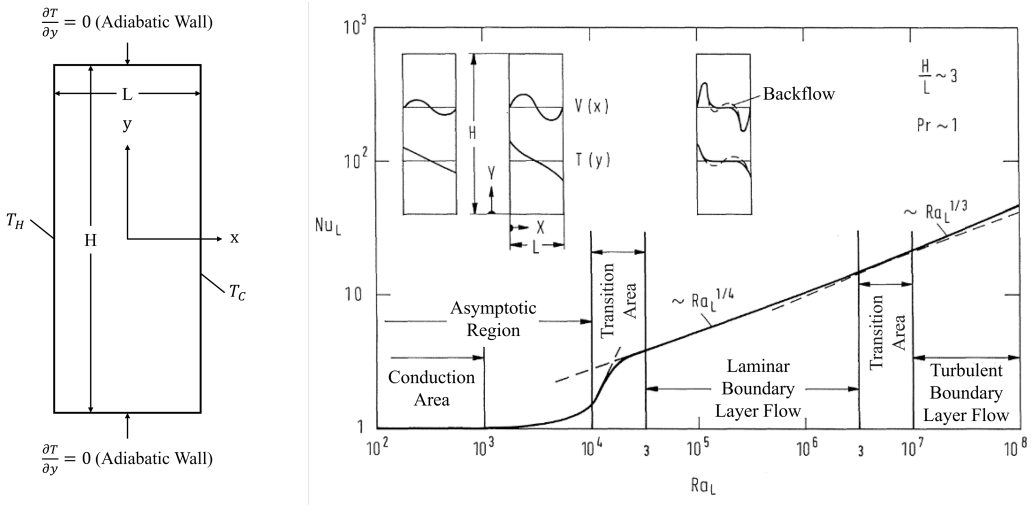


Figure 1.1: Qualitative progression of the Nusselt number (Nu_L) depending on the Rayleigh number (Ra_L) for vertical confined spaces, translated from [29]

1.2 Thermal Ignition

Combustion of hydrocarbon fuels is typically divided into slow reaction, cool flame, and ignition regimes [36]. The time-dependent process in which reactants evolve over time into a steadily burning flame is called ignition. Thermal ignition is the phenomenon where a substance ignites without an external ignition source such as a flame or spark, and the required energy is instead supplied via thermal heating. A thermal explosion can occur in a closed volume containing a combustible mixture when the rate of heat production due to chemical reactions surpasses the rate of heat loss through the vessel's walls. This phenomenon is known as the thermal explosion limit, or the third explosion limit [37]. Energy loss occurs through heat transfer in the form of conduction, convection, and radiation.

Several standardized tests have been developed to characterize the hazard potential of ignition. For instance in many industries, including aviation, the ASTM-E659 test standard is widely used [2]. However, this test may not be appropriate for many configurations such as the Hele-Shaw geometry and the methodology has been criticized in recent studies [11, 15, 20].

1.3 Research Objectives

In light of what has been discussed in the preceding sections and to bridge the research gap, the present thesis aimed at:

- Applying the Hele-Shaw approximations to reacting flows of combustible gases.
- Developing a new solver in OpenFOAM with the Hele-Shaw approximations.
- Investigating fluid dynamics in the Hele-Shaw cells with large temperature differences (600 K).
- Studying and analyzing the ignition dynamics in the Hele-Shaw cells.

1.4 Scope of present work

In the present work, the fundamentals that will be later used to define the implemented solvers will be introduced in Chapter 2. Especially, the proof of a parabolic velocity profile over the gap, also referred to later as Hele-Shaw approximations is an important part of the Chapter. The investigated problem with the described geometry and boundary conditions is introduced in Chapter 3. The numerical setup and methodology for the fluid and ignition dynamics are introduced in Chapter 4 and 5. The results are presented and discussed in Chapter 6. In this Chapter the Hele-Shaw approximations and the newly implemented solver are validated, the results of the fluid dynamics simulations with air and without chemistry, and the simulations results of hot surface ignition are presented. The conclusions are presented in Chapter 7. Fig. 1.2 provides the methodology flowchart followed in this study.

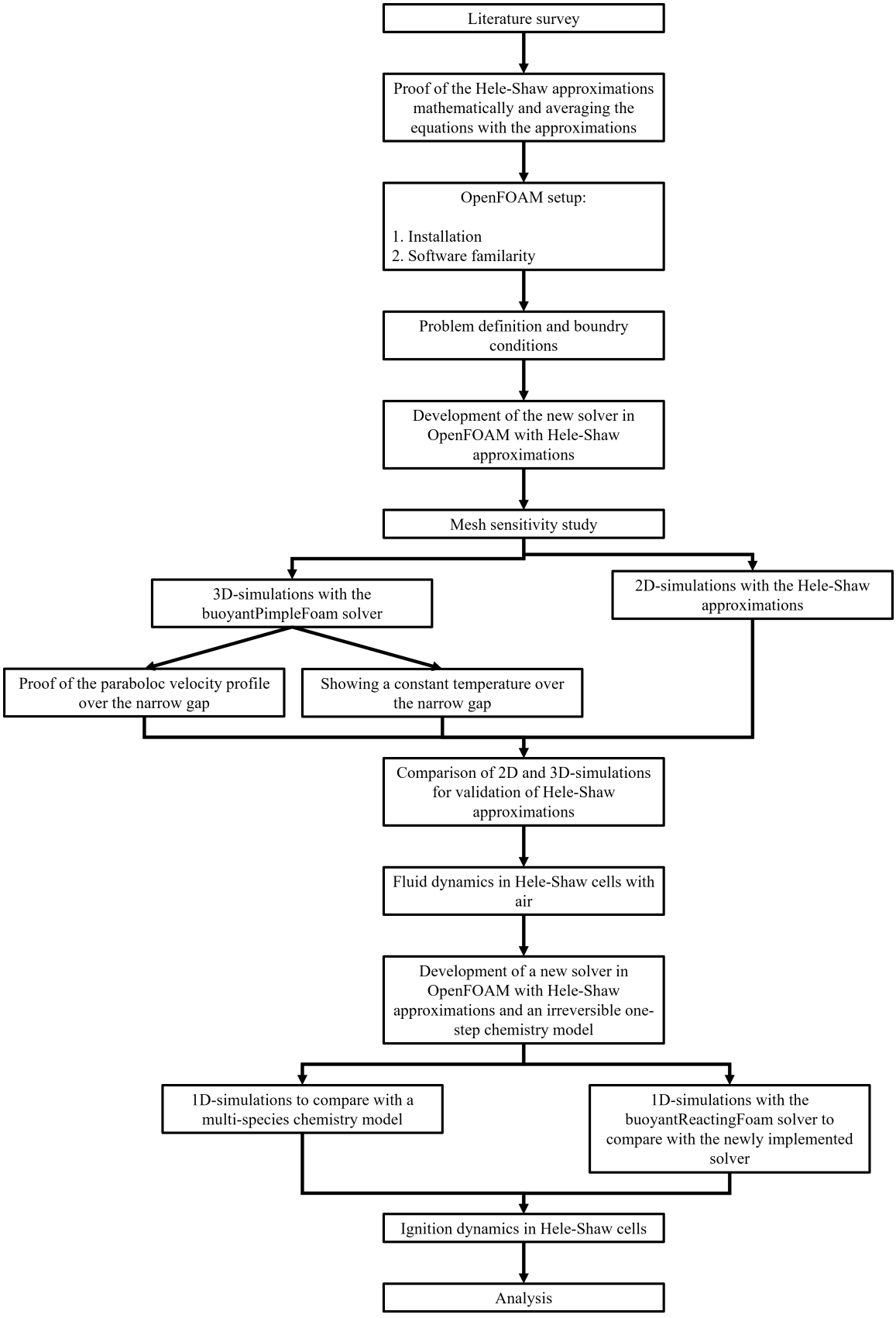


Figure 1.2: Methodology flowchart of the present study

2 Fundamentals

This chapter introduces the fundamentals that will be later used in this study. The Hele-Shaw approximations involve a parabolic velocity profile across the narrow gap, resulting in the set of equations being averaged over the gap.

2.1 Non-Boussinesq Natural Convection

Most existing work on natural convection in Hele-Shaw cells has been done using the Boussinesq approximation (described Sec. 2.1.1). However, as described in Sec. 2.1.1, because large temperature differences are one of the main aspects of the present work, the Boussinesq approximation does not apply.

2.1.1 Boussinesq Approximation

In the Boussinesq approximation, it is considered that the change in density is linearly proportional to the change in temperature:

$$\rho = \rho_0(1 - \alpha(T - T_0)) \tag{2.1}$$

where α is the coefficient of thermal expansion, ρ is the density, ρ_0 is the absolute density, T is the temperature, and T_0 is the absolut temperature.

From Tritton [34], the conditions for the Boussinesq approximation to hold are as follows:

$$\alpha\theta << 1 \tag{2.2}$$

$$g\rho\zeta L << 1 \tag{2.3}$$

$$g\alpha L/c_p L << 1 \tag{2.4}$$

$$\frac{g\alpha L T_0}{c_p \theta} << 1. \tag{2.5}$$

where ζ is the isothermal compressibility, c_p is the heat capacity at constant pressure, L is the length scale, and g is the acceleration of gravity.

Condition Eq. (2.2) derives from checking whether variations in ρ are small concerning the temperature. If $\alpha\theta << 1$, then $\rho \cong \rho_0$. In addition, if $\alpha\theta$ is sufficiently large, other fluid properties (i.e., viscosity, specific heat, etc.) cannot be considered constant. Condition Eq. (2.3) is a check to ensure variations in ρ with respect to the hydrostatic pressure are small. For example, if Earth's atmosphere were the configuration of interest, there would be large density variations caused purely by hydrostatic effects. Both conditions

Eq. (2.4) and Eq. (2.5) are similar in that they deal with pressure contributions in the energy equation. Condition Eq. (2.4) is a check to ensure negligible hydrostatic pressure contributions to the energy. Condition Eq. (2.5) is an equivalent statement to condition Eq. (2.4). However, instead of looking at the hydrostatic pressure, it instead looks at the pressure fluctuations caused by the fluid motion. This must also be negligible to fully utilize the Boussinesq approximation. If conditions Eq. (2.2) - Eq. (2.5) hold, the Boussinesq approximation applies directly. If only conditions Eq. (2.2) - Eq. (2.4) hold (but condition Eq. (2.5) does not), the approximation can be applied with the variable temperature, T, being replaced by the potential temperature.

2.2 Parabolic Velocity Shape Across the Gap

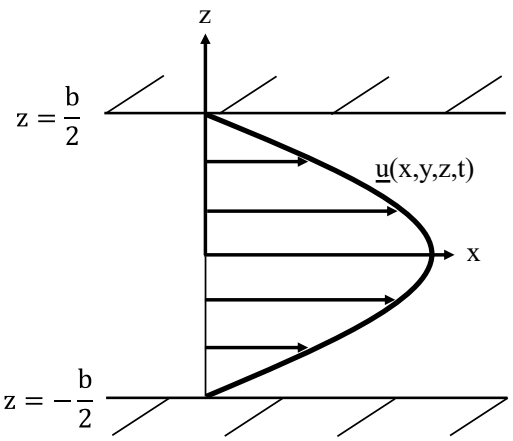


Figure 2.1: Parabolic velocity profile over the gap

In existing studies of flow in a Hele-Shaw cells, the velocity profile across the gap is assumed to be parabolic in order to reduce the problem to two dimensions as shown in Fig. 2.1. Nevertheless, none of the existing studies in the open literature provide proof through detailed analysis or comparison with solutions to the three dimensional flow. Furthermore, previous studies assume constant density or steady-state conditions. Therefore, it is necessary to establish that a parabolic velocity profile across the gap remains valid even for non-steady flows and variable density. The derivation of the Hele-Shaw approximation starts from the Navier-Stokes equation including buoyancy force:

$$\rho\left(\frac{\partial \underline{u}}{\partial t} + \underline{u} \cdot \nabla \underline{u}\right) = -\nabla p + \mu \nabla^2 \underline{u} + \rho \underline{g} \tag{2.6}$$

where ρ, $\underline{u}$, p, μ, and $\underline{g}$ are the density, flow velocity, pressure, dynamic viscosity, and body accelerations (gravity).

It can be assumed that there is no flow in the z-direction, given the symmetry and conditions on the velocity at the xy planes. The convective term $\underline{u} \cdot \nabla \underline{u}$ may be neglected in the Navier-Stokes equation since the flow is in a thin film [1]. In this case, the Reynolds number does not have to be low to neglect the $\underline{u} \cdot \nabla \underline{u}$ term. Due to the small gap and the

no-slip boundary condition at the walls, the flow velocity at the walls is zero. Symmetry in the z-direction ensures that the maximum velocity occurs at the center of the gap. These significant changes in velocity in the z-direction lead to velocity gradients in the z-direction being much larger than those in the x- and y-directions. Therefore the $\nabla^2\underline{u}$ term is reduced to:

$$\nabla^2\underline{u} \cong \frac{\partial^2 u}{\partial z^2}\underline{e}_x + \frac{\partial^2 v}{\partial z^2}\underline{e}_y \tag{2.7}$$

The $\partial\underline{u}/\partial t$ term is proportional to U^2/H for laminar flows, where U is the characteristic velocity, H is the characteristic height [1]. This proportionality shows that compared to the $\nabla^2\underline{u}$ term, the $\partial\underline{u}/\partial t$ term can be neglected as long as:

$$\rho\frac{UH}{\mu}(\frac{b}{H})^2 = Re_H(\frac{b}{H})^2 << 1 \tag{2.8}$$

holds. With all of these introduced simplifications the Navier-Stokes equation in a Hele-Shaw cell can be written as:

$$\frac{\partial p}{\partial x} = \mu\frac{\partial^2 u}{\partial z^2} \tag{2.9}$$

$$\frac{\partial p}{\partial y} = \mu\frac{\partial^2 v}{\partial z^2} - \rho g \tag{2.10}$$

$$\frac{\partial p}{\partial z} = 0 \Rightarrow p = p(x, y, t) \tag{2.11}$$

Eq. (2.11) implies that the pressure is not dependent on z. For Eq. (2.9) and (2.10), one may notice that on the left-hand side no dependency on z exists while on the right-hand side, there is a dependency on z. Therefore, one can easily solve the partial equations:

$$u(x, y, z, t) = \frac{1}{2\mu}\frac{\partial p}{\partial x}z^2 + Az + B \tag{2.12}$$

$$v(x, y, z, t) = \frac{1}{2\mu}\frac{\partial p}{\partial y}z^2 + Cz + D \tag{2.13}$$

as a result, the velocity is shown to be parabolic across the gap. Using the no-slip boundary condition ($u(x, y, z = -b/2, t) = u(x, y, z = b/2, t) = v(x, y, z = -b/2, t) = v(x, y, z = b/2, t) = 0$) A, B, C, and D can be determined. The Eqs. (2.12) and (2.13) can be now rewritten:

$$u(x, y, z, t) = \bar{U}(x, y, t)f(z) \tag{2.14}$$

$$v(x, y, z, t) = \bar{V}(x, y, t)f(z) \tag{2.15}$$

with:

$$f(z) = \frac{3}{2}\left[1 - \left(\frac{2}{b}\right)^2 z^2\right] \tag{2.16}$$

and

$$< f(z) >= \frac{1}{b}\int_{-b/2}^{b/2} f(z)dz = 1 \tag{2.17}$$

$$< f(z)^2 >= \frac{1}{b}\int_{-b/2}^{b/2} f(z)^2 dz = 1.2 \tag{2.18}$$

here, $\bar{U}$ and $\bar{V}$ represent two-thirds of the maximum velocity components in the x-direction (u) and the y-direction (v), respectively.

The key point here is that by averaging in the z-direction, the problem can be reduced to two dimensions without assuming constant density or steady-state conditions. For the parabolic velocity profile to be valid, it would be sufficient that conditions such as the small gap assumption ($b/h << 1$ and $b/l << 1$) as well as Eq. (2.8) are met. Later in Sec. 6.1.1 this will be shown with simulations.

2.3 Governing Equations

As described in Sec. 2.2, a parabolic velocity profile over the gap is considered to derive the governing equations implemented in OpenFOAM. By averaging in the z-direction, and assuming that density (ρ), temperature (T), and mass fraction (Y_i) are not dependent on the z-direction (explained in Sec. 6.1.2) then the relevant equation set is as follows:

$$\frac{\partial U}{\partial t} + 1.2(U\frac{\partial U}{\partial x} + V\frac{\partial U}{\partial y}) = -\frac{1}{\rho}\frac{\partial p}{\partial x} + \nu(\nabla_0^2 U - \frac{1}{K}U) \tag{2.19}$$

$$\frac{\partial V}{\partial t} + 1.2(U\frac{\partial V}{\partial x} + V\frac{\partial V}{\partial y}) = -\frac{1}{\rho}\frac{\partial p}{\partial y} + \nu(\nabla_0^2 V - \frac{1}{K}V) - \rho g \tag{2.20}$$

$$\frac{\partial \rho}{\partial t} + \nabla_0 \cdot (\rho \underline{U}) = 0 \tag{2.21}$$

$$\frac{\partial \rho Y_R}{\partial t} + \nabla_0 \cdot (\rho \underline{U} Y_R) = -\nabla_0 \cdot \underline{j}_R + \dot{\Omega}_R \tag{2.22}$$

$$\frac{\partial (\rho h_s)}{\partial t} + \nabla \cdot (\kappa / c_p \nabla h_s) + q_c \dot{\Omega}_R \tag{2.23}$$

where K is

$$K = \frac{1}{12}b^2, \tag{2.24}$$

and ∇_0 is defined as

$$\nabla_0 = \frac{\partial}{\partial x}\underline{e}_x + \frac{\partial}{\partial y}\underline{e}_y \tag{2.25}$$

In Eqs. 2.19-2.22, h_s is the sensible enthalpy, c_p is the specific heat capacity at constant pressure, $\underline{j}_R$ is the diffusive mass flux of the reactants, Y_R is the mass fraction of the reactants, $\dot{\Omega}_R$ is the production rate for the reactants, κ is the thermal conductivity, q_c is the stored chemical energy, and ν is the kinematic viscosity. Fick's law with unity Lewis number was used for species diffusion, such that $\underline{j}_R = -\kappa / c_p \nabla Y_R$.

With Eqs. 2.19, and 2.20 the problem reduces to a two-dimension model without losing information of the velocity in the z-direction. It is also to be noted that the assumption that the mass fraction, density, and temperature are constant over the gap is only possible when there is no thermal or material diffusion at the walls, which is true for the configurations studied in this thesis.

3 Problem Statement

This section outlines the problem of ignition analysis, as defined in the present study. The considered arrangements are shown in Fig. 3.1 in which the xy- and xz-planes are adiabatic. The yz-plane on the left side is isothermal with a temperature of T_H (900 K), and the yz-plane on the right side is also isothermal with the temperature T_C (300 K), $T_H > T_C$. The initial temperature of the air in the simulations without chemistry was 300 K. All walls are set to no-slip conditions (no velocity at the walls). The gap, b, is small compared to l and h ($b/h << 1$ and $b/l << 1$) which satisfies the Hele-Shaw approximations with a length of 0.005 m for the length magnitudes studied in this thesis (Sec. 6.1.1).

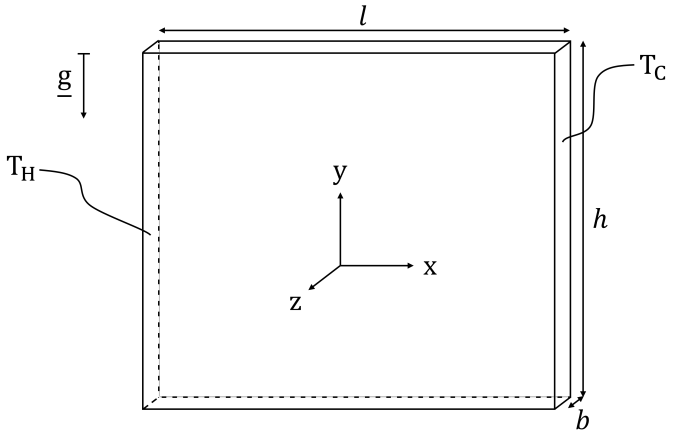


Figure 3.1: Diagram of the Hele-Shaw Cell

First, the natural convection in the thin confined space such as the Hele-Shaw cells with large temperature differences (600 K) and nonreactive flow was studied. Understanding the nonreactive flow regimes is indispensable for interpreting the results of the ignition study. Simulations were conducted using the approximations described in Sec. 2.2 and the governing equations presented in Sec. 2.3. To do this, a new solver was implemented in OpenFOAM andverified against three-dimensional simulations (Sec. 6.1).

Once the flow regimes are discerned then the chemical reactions of n-hexane have to be studied and added to the simulations. Hexane is an appropriate fuel to study ignition since it has a similar autoignition temperature (498 K, based on the ASTM E659 standard [22], [30]) as aviation-grade kerosene known as Jet A (511 K, based on the ASTM E659 standard). As briefly discussed in Sec. 1.2 in previous analysis work on the ASTM-E659 standardized test it has been observed that the standard is not an appropriate way to determine the autoignition temperature. However, it could still be used as an indicator for similar hexane and jet fuel combustion behaviors. Moreover, the chemical reactions of n-hexane are not

as complex as those for jet fuel, and detailed chemical reaction mechanisms are available[1]. Thereafter, the ignition delay time and position for different Hele-Shaw configurations must also be studied. The initial pressure for the simulations without chemistry and just air to study the fluid dynamics is set initially to 10^5 Pa. The simulations with chemistry with a stoichiometric air and n-hexane mixture to study the ignition dynamics are started from the steady solution (if not stated otherwise) of the simulation results with air alone.

3.1 Assumptions and Simplifications

Previous studies have concluded that the heating rate also influences thermal ignition [5, 27]. However, in the present work, the wall conditions were set from the outset to the specified parameters, and the effect of the heating rate was not considered. Radiation is also neglected. In the fluid dynamics simulations with just air, air is modeled as an ideal gas. In the simulations with a stoichiometric air and n-hexane mixture, and with chemistry to capture ignition the fluid is modeled as a perfect gas.

[1] On Professor Shepherd's website the different mechanisms are introduced: `https://shepherd.caltech.edu/EDL/PublicResources/sdt/cti_mech.html`

4 Numerical Setup and Methodologies for Fluid Dynamics

This chapter outlines the numerical setup and methodology used for the analysis of the fluid dynamics in the Hele-Shaw cell. In Chapter 5 the numerical setup and methodology used to predict ignition will be elucidated. In this study, the software framework OpenFOAM [33] was used to numerically investigate computational fluid dynamics (CFD) in the thin compartment. As there was not an existing solver in OpenFOAM for a Hele-Shaw cell that solves the problem effectively in terms of computational time and is also applicable for various cases considered in this study, a new solver had to be implemented. The new solver is native to the toolbox `buoyantPimpleFoam` solver, and is called `Adiabatic_heleShawFoam` and is based on the Hele-Shaw equations presented in Chapter2.1.1 and the extension to heat transfer discussed in [17].

4.1 Transport Model

In OpenFOAM, the Sutherland law is commonly used to model the temperature dependency of dynamic viscosity for gases[1]. Accordingly, the transport model can be expressed for the dynamic viscosity (μ) in the following form:

$$\mu = A_s \frac{\sqrt{T}}{1 + T_s/T} \tag{4.1}$$

here A_s and T_s denote the model coefficients. The thermal conductivity κ is given by the modified Eucken relation:

$$\kappa = \mu c_v (1.32 + 1.77 \frac{R}{c_v}) \tag{4.2}$$

where c_v is the heat capacity at constant volume and R is the universal gas constant.

To check the validity and accuracy of the Sutherland law in the temperature range investigated in this study, μ and κ were also determined by Cantera [16]. Cantera is an open-source suite of tools for problems involving chemical kinetics, thermodynamics, and transport processes. Cantera uses thermodynamic data in the form of NASA polynomials, which are derived from experimental data. Cantera is widely accepted and used in the combustion field. As shown in Fig. 4.1 the Sutherland law predicts for lower temperatures a value close to the results from Cantera. At elevated temperatures, the discrepancy between the Sutherland law and the results from Cantera increases. For the current study, for a more precise transport model, the "polynomial"[2] transport model in OpenFoam is used

[1] https://doc.openfoam.com/2306/tools/processing/models/thermophysical/transport/rtm/sutherland/

[2] `https://doc.openfoam.com/2312/tools/processing/models/thermophysical/transport/rtm/polynomial/`

instead of the "Sutherland"[3] transport model. In the "polynomial" transport model μ is defined as:

$$\mu = \sum_{i=1}^{N} (c_i T^{i-1}) \tag{4.3}$$

and similarly κ is defined by

$$\kappa = \sum_{i=1}^{N} (c_i T^{i-1}) \tag{4.4}$$

The fitting coefficients are given in Table 4.1. The comparison of the Sutherland law to the calculated viscosity by Canetra is illustrated in Fig. 4.1. From the visual comparison, it is evident that the deviation of the Sutherland law from the calculated viscosity increases.

Table 4.1: Coefficients for the transport model in OpenFOAM

	c_1	c_2	c_3	c_4	c_5	c_6	c_7	c_8
μ	1.3604e-06	7.2697e-08	-6.2883e-11	5.2483e-14	-2.8448e-17	9.3468e-21	-1.6875e-24	1.2818e-28
κ	0.0066	6.5173e-5	6.9374e-9	-1.7561e-11	1.1531e-14	-4.0850e-18	7.6671e-22	-5.9616e-26

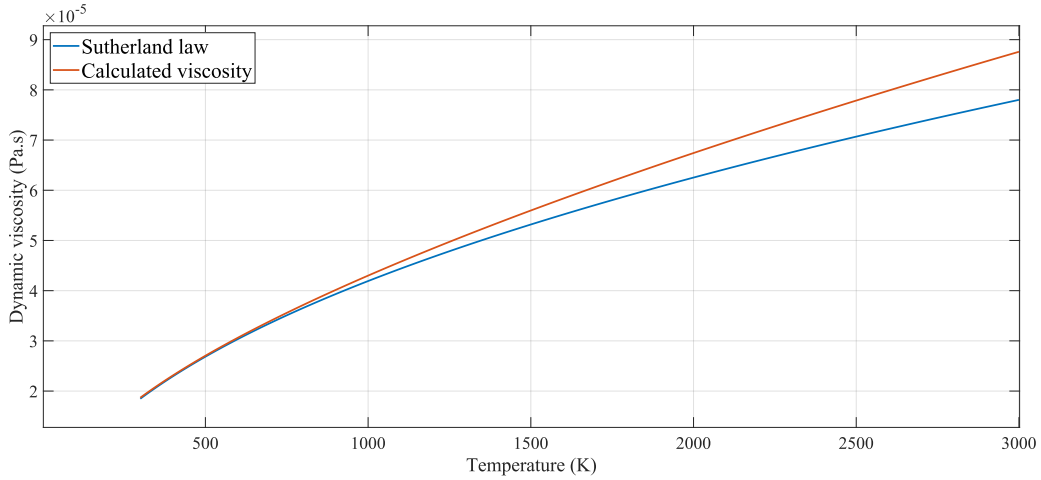


Figure 4.1: Comparison of the Sutherland law to the calculated viscosity by Canetra with $A_s = 1.4792e-6\ K^{-0.5}s^{-1}m^{-1}kg$ and $T_s = 116$ K

4.2 Thermodynamic Property Characteristics

The JANAF (Joint Army-Navy-Air Force) model provides thermodynamic property characteristics as a function of temperature often used for high-temperature gas dynamics

[3] https://doc.openfoam.com/2312/tools/processing/models/thermophysical/transport/rtm/sutherland/

simulations, where properties vary significantly with temperature. The empirical equations are given as follows:

$$\text{Heat capacity: } \frac{c_p^0(T)}{R} = a_1 + a_2T + a_3T^2 + a_4T^3 + a_5T^4 \tag{4.5}$$

$$\text{Enthalpy: } \frac{H^0(T)}{RT} = a_1 + a_2\frac{T}{2} + a_3\frac{T^2}{3} + a_4\frac{T^3}{4} + a_5\frac{T^4}{5} + \frac{b_1}{T} \tag{4.6}$$

$$\text{Entropy: } \frac{S^0(T)}{R} = a_1 lnT + a_2T + a_3\frac{T^2}{2} + a_4\frac{T^3}{3} + a_5\frac{T^4}{4} + b_2 \tag{4.7}$$

In OpenFOAM, there are two sets of data that need to be given one is for low temperatures (T < 1000 K), and one for high temperatures (T > 1000 K)[4]. Since there are different coefficients for air given in CFD forums and literature, the coefficients were recalculated for the present study. The Nitrogen (N_2), Oxygen (O_2), and Argon (Ar) coefficients were used from the tables given by NASA Glenn documentation [26]. With these coefficients, the air coefficients were calculated by averaging with 78 % Nitrogen, 21 % Oxygen, and 1 % Argon. The calculated coefficients for the high- and low-temperature coefficients are given in Table 4.2, and Table 4.3. The calculated coefficients are similar to those given in the NASA database[5]. It could also be shown that the plot of the heat capacity, enthalpy, and entropy are continuous for T=1000 K, and the derivative is also the same for the right and left side of T=1000 K (Fig. 4.2). This indicates that the calculated coefficients are accurate. The heat capacity c_p^0 also indicates that the parameters are correct. Nitrogen which is the main component of air by concentration has a degree of freedom of seven for low temperatures, and for higher temperatures a degree of freedom of nine. Therefore, the heat capacity for low temperatures should be 3.5, and for higher temperatures 4.5, as can be seen in Fig. 4.2a [19].

Table 4.2: JANAF high-temperature coefficients

	a_1	a_2	a_3	a_4	a_5	b_1	b_2
N_2	2.95257625e0	1.39690057e-3	-4.92631691e-7	7.86010367e-11	-4.60755321e-15	-9.2394864e2	5.87189252e0
O_2	3.66096083e0	6.56368523e-4	-1.41149488e-7	2.06797688e-11	-1.29913248e-15	-1.21697725e3	3.41536184e0
Ar	2.5	0	0	0	0	-7.45375e2	4.37967491e0
Air	3.09681125	1.22741984e-3	-4.13894111e-7	6.56515600e-11	-3.866709325e-15	-9.83698912e2	5.34109890e0

4.3 Mesh Sensitivity Study

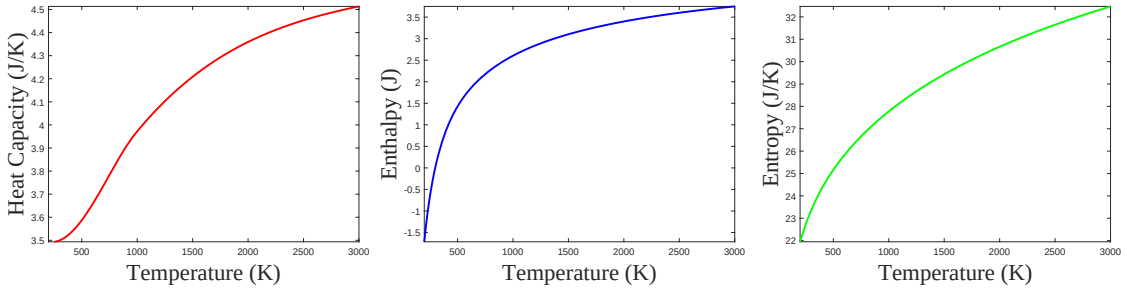
One prerequisite condition for running a CFD simulation is to split the computational domain into several discrete mesh cells. The governing flow equations and other models are applied in a simulation, and the results are calculated using the mesh as a base. This

[4] https://doc.openfoam.com/2306/tools/processing/models/thermophysical/thermodynamics/rtm/janaf/

[5] https://shepherd.caltech.edu/EDL/PublicResources/sdt/SDToolbox/cti/NASA7/nasa7mod.dat

Table 4.3: JANAF low-temperature coefficients

	a_1	a_2	a_3	a_4	a_5	b_1	b_2
N_2	3.53100528e0	-1.23660987e-4	-5.02999437e-7	2.43530612e-9	-1.40881235e-12	-1.04697628e3	2.96747468e0
O_2	3.78245636e0	-2.99673415e-3	9.84730200e-6	-9.68129608e-9	3.24372836e-12	-1.06394356e3	3.65767573e0
Ar	2.5	0	0	0	0	-7.45375e2	4.37967491e0
Air	3.57349995	-7.25769741e-4	1.67559386e-6	-1.33533403e-10	-4.17690677e-13	-1.04752339e3	3.12653890e0



(a) Heat capacity (b) Enthalpy (c) Entropy

Figure 4.2: Thermodynamic properties based on the JANAF model

process will result in spatial discretization errors. Therefore, a mesh sensitivity study (also known as a mesh independence or mesh convergence study) has to be carried out. A mesh sensitivity study consists of running the same simulation using grids with different resolutions and analyzing how much the solution changes with each mesh. The main purpose of a grid convergence study is to obtain an optimum grid size so that the accuracy of the solution is independent of the computational grid. Therefore, the two parameters considered are the number of cells and the expansion ratio (described in Sec. 4.3.2).

For the mesh sensitivity analysis, a Hele-Shaw cell with a size of $h = 0.3$ m, $l = 0.1$ m, and $b = 0.005$ m were chosen. Hele-Shaw cell simulations with different numbers of grids per length (same grid density for height and length) were conducted with the Adiabatic_heleShawFoam solver. The grid size in the x- and y-direction is uniform (Sec. 4.3.1). Later in Sec. 4.3.2, the expansion ratio in the x- and y-direction will change with a constant number of cells. Based on the analysis's results, a cell number of 60 per 10 cm with an expansion ratio of 20 in the x-direction and 10 in the y-direction was chosen for a decent computing time and small deviations to the finest mesh. In Fig. 4.3 a Hele-Shaw cell with the described mesh configuration is illustrated.

A mesh sensitivity analysis for the three-dimensional simulations similar to the previously described two-dimensional analysis was conducted. Since the gradients of the velocity components are relatively steep, a large number of cells are necessary to capture the gradients correctly. In the x and y-direction, the same cell sizes as in the two-dimensional simulation were used, and the cell size in the gap direction (z-direction) was 142.86 μm or 35 uniform cells in the gap length of 0.005 m.

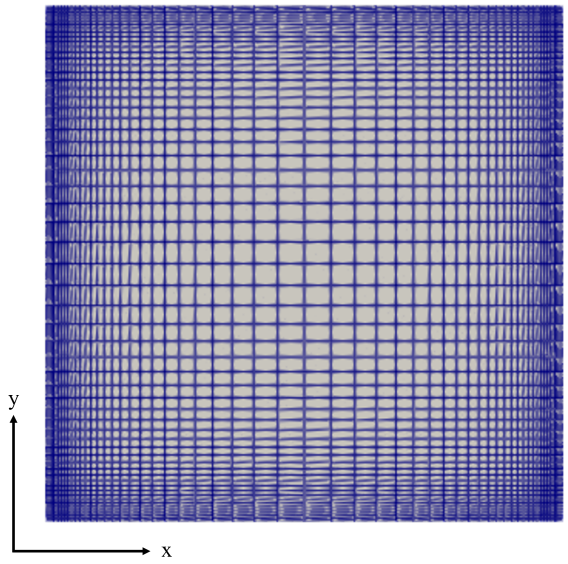


Figure 4.3: Optimal computational domain for a Hele-Shaw cell with dimensions of 0.1 m in both height and length and a gap size of 0.005 m with cell compression near the walls

4.3.1 Number of Cells

In order to give a more comprehensive analysis, specific points in the domain (Sec. 4.3.1.2) were analyzed, and for a global parameter, the L2-error norm was computed (Sec. 4.3.1.1). All Simulations in this section have been conducted with a uniform grid size (unity expansion ratio).

4.3.1.1 Global Analysis

To quantify the global mesh sensitivity the L2-error norm, also referred to as the Root Mean Squared Error, was calculated. As a reference case, the simulation with 300 cells per 10 cm was chosen (also referred to as fine mesh). Since the cell locations of the different cases are not the same as the locations in the fine mesh, an interpolation of the fine mesh in Matlab with the "scatteredInterpolant"[6] function was done. The L2-error norm is given as:

$$L_2 \text{ error norm: } \|X\|_2 = \sqrt{\frac{1}{N}\sum_i (X_{i,coarsemesh} - X_{i,finemesh})^2} \tag{4.8}$$

where N is the number of cells of the coarse mesh, and X is either one of the velocity components or the temperature. A value closer to zero indicates that the model has a smaller deviation from the reference mesh.

Fig. 4.4 displays the L2-error norm for the different amounts of cells. Due to the uniform grid, no additional weighting is applied to any area of the domain.

[6] https://www.mathworks.com/help/matlab/ref/scatteredinterpolant.html

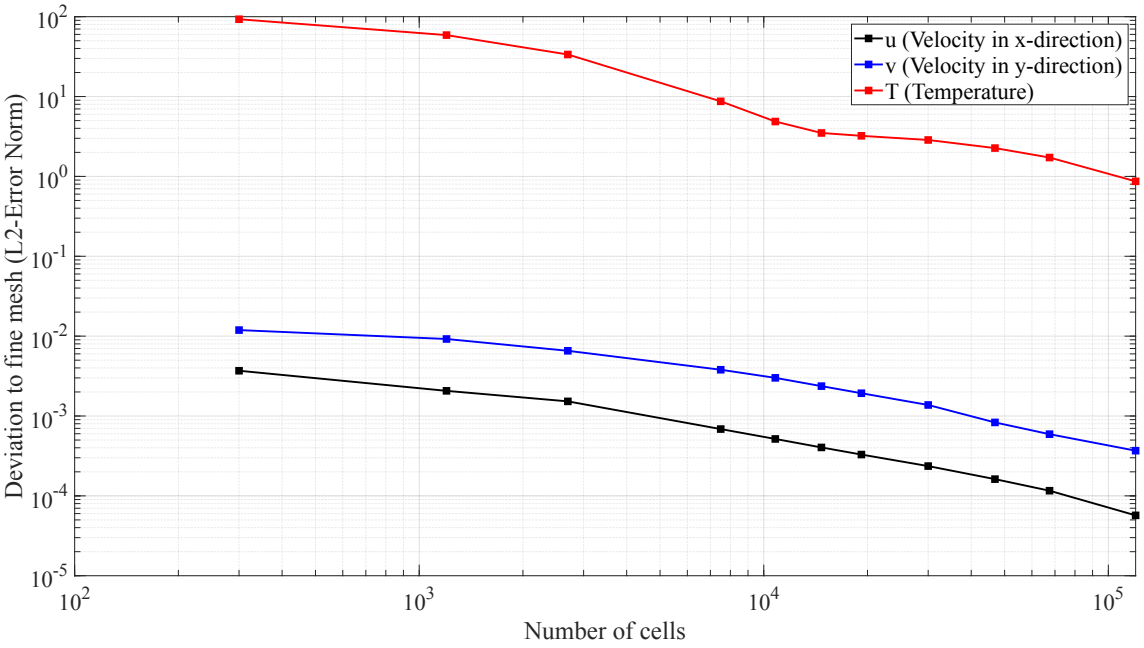


Figure 4.4: Global mesh sensitivity with a uniform grid

4.3.1.2 local Analysis

Three points were chosen for the local analysis (Later referred to as points A, B, and C). The first one is in $\underline{x}_A = (0.005, 0.05)$ m, another one is in the middle of the cell $\underline{x}_B = (0.05, 0.15)$ m, the last one is in $\underline{x}_C = (0.075, 0.225)$ m. As an indicator of the convergence the deviation to finest mesh, which is 300 cells per 10 cm is chosen. The following equation gives the deviation in percent:

$$\text{Deviation to fine Mesh} = \left(\frac{X_{i,coarsemesh}}{X_{i,finemesh}} - 1\right) * 100\% \tag{4.9}$$

The local analyses are given in Fig. 4.5. The higher deviations of the velocity in the x-direction (u) visible in Fig. 4.5a are connected with lower speeds compared to the velocity in the y-direction.

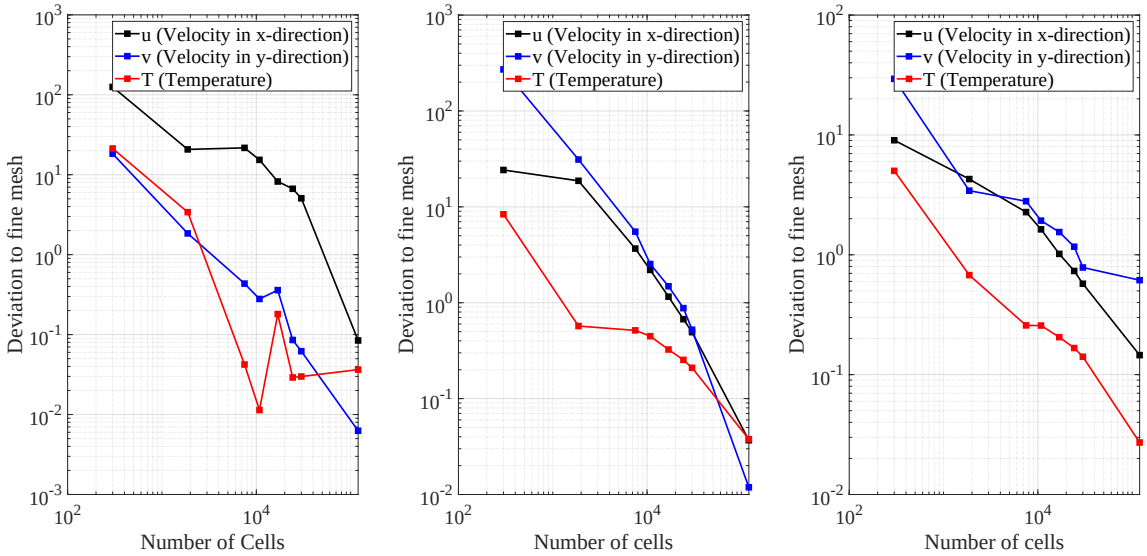
4.3.2 Expansion Ratio

The expansion ratio is defined as the length of the longest cell to the smallest, illustrated in Fig. 4.6. The scaling of the lengths is geometric. The cell-to-cell expansion ratio (a) is given by:

$$a = E^{\frac{1}{n-1}} \tag{4.10}$$

where E is the expansion ratio, and n is the number of cells. The width of the shortest cell (δ_s), and of the longest cell (δ_e) is given by:

$$\delta_s = \frac{l(a-1)}{a^n - 1} \tag{4.11}$$



(a) Mesh Sensitivity at $\underline{x}_A = (0.005, 0.05)$ m (b) Mesh Sensitivity at $\underline{x}_B = (0.05, 0.15)$ m (c) Mesh Sensitivity at $\underline{x}_C = (0.075, 0.225)$ m

Figure 4.5: Local Mesh Sensitivity Analysis

$$\delta_e = E\frac{l(a-1)}{a^n - 1} \tag{4.12}$$

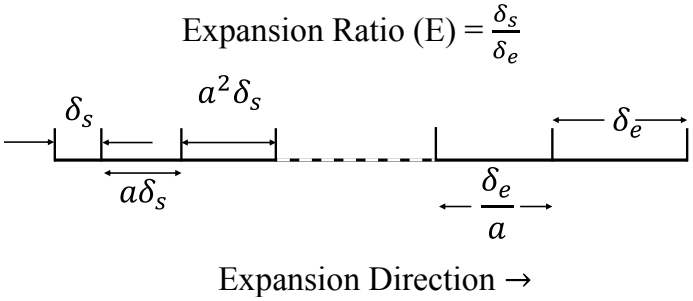
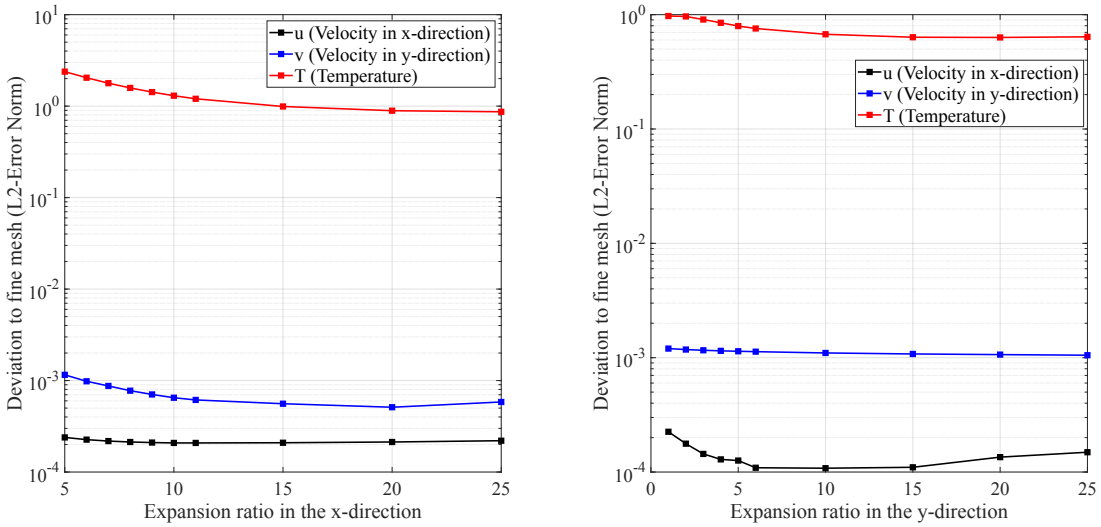


Figure 4.6: Mesh grading along a block edge

From the results of Sec. 4.3.1, the chosen number of cells per 10 cm is 60. To keep the computation time approximately the same, and make the deviation to the finest simulated mesh smaller, the effect of the expansion ratio on the deviation has been studied. The grading of the cell size in this study is implemented in a way that the cells in the middle are the longest, and towards the right and left walls, it gets refined[7]. A higher mesh density is required close to the walls since the boundary layers are closer in this regions than in the middle of the domain. Similar to Sec. 4.3.1 a local- and global analysis has been done. As the reference velocity and temperature, the result of the simulation with 300 cells per 10 cm was chosen similar to Sec. 4.3.1. The L2-error norm is displayed in Fig. 4.7 for

[7]The code was obtained from page 33 of: `https://www.wolfdynamics.com/wiki/meshing_OF_blockmesh.pdf`

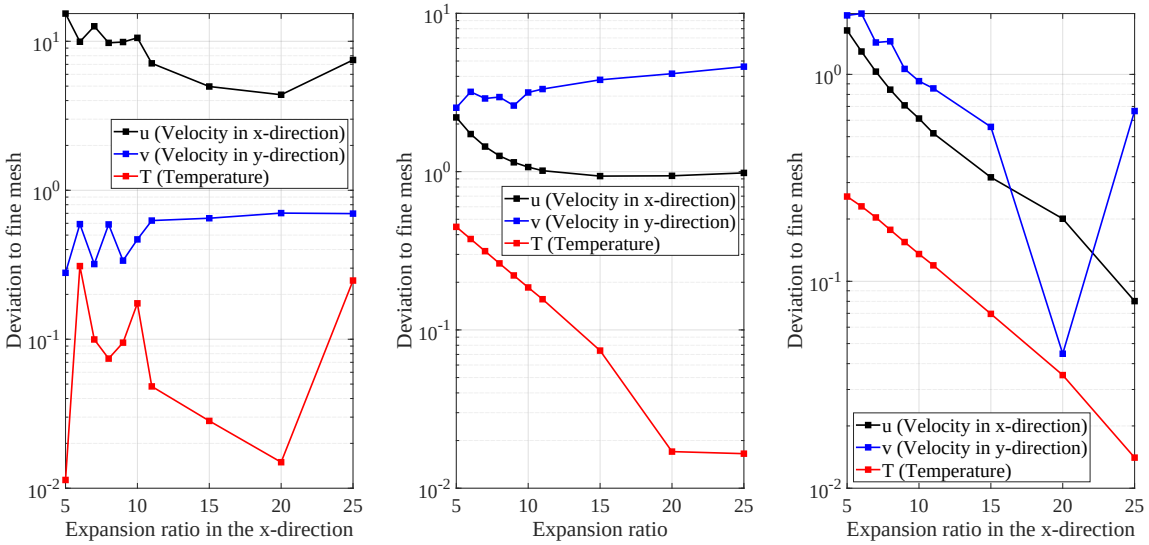
expansions in the x- and y-direction. The local deviations are illustrated in Figs. 4.8 and 4.9, with the same A, B, and C coordinates described in Sec. 4.3.1.2.



(a) Mesh sensitivity analysis with varying expansion ratio in the x-direction, and with an expansion ratio in the y-direction of 1

(b) Mesh sensitivity analysis with varying expansion ratio in the y-direction, and with an expansion ratio in the x-direction of 20

Figure 4.7: Global mesh sensitivity analysis with varying expansion ratios

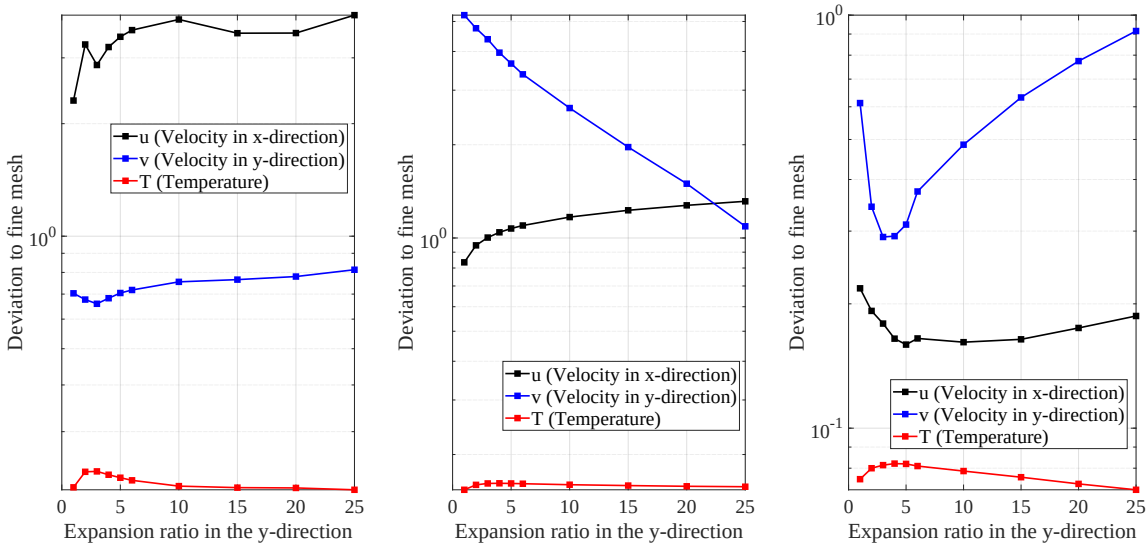


(a) Mesh Sensitivity at $\underline{x}_A = (0.005, 0.05)$

(b) Mesh Sensitivity at $\underline{x}_B = (0.05, 0.15)$

(c) Mesh Sensitivity at $\underline{x}_C = (0.075, 0.225)$

Figure 4.8: Local Mesh Sensitivity Analysis with varying expansion ratio in the x-direction, and with an expansion ratio in the y-direction of 1



(a) Mesh Sensitivity at $\underline{x}_A = (0.005, 0.05)$

(b) Mesh Sensitivity at $\underline{x}_B = (0.05, 0.15)$

(c) Mesh Sensitivity at $\underline{x}_C = (0.075, 0.225)$

Figure 4.9: Local Mesh Sensitivity Analysis with varying expansion ratio in the y-direction, and with an expansion ratio in the x-direction of 20

5 Numerical Setup and Methodology for Ignition Dynamics

The newly implemented solver, `ReactingHeleShawFoam`, in OpenFOAM is based on the `Adiabatic_heleShawFoam` solver. It contains the Hele-Shaw assumptions described in Chapter 4. In addition, the new solver considers chemistry as well and is native to the basic `bouyantReactingFoam` solver. The chemistry is modeled using an irreversible one-step scheme (R $\rightarrow$ P). The fluid was modeled as a stoichiometric air and n-hexane mixture (2.16 % mole fraction of n-hexane, 20.56 % mole fraction of oxygen, and 77.28 % mole fraction of nitrogen) at a pressure of one bar and a temperature of 300 K. Air and n-hexane are assumed to be perfect gases. The constants were gathered from Schoeffler et al work [31], which also used the same chemistry model to model a stoichiometric air and n-hexane mixture with the same conditions as in the present study. These constants are given in Table 5.1. Since the heat capacity is assumed to be constant, hence at constant pressure (C_p) is equal to a_1 in Eq. 4.5. For the enthalpy and entropy b_1 and b_2 are given in Table 5.1.

The one-step reaction mechanism described in Schoeffler's work was defined using a modified Arrhenius rate law:

$$k(T) = AT^{\alpha} \exp\left(-\frac{E_a}{RT}\right) \tag{5.1}$$

where k, T, E_a, R, and A are the rate constant, the temperature, the activation energy, the universal gas constant, and a pre-exponential factor also referred to as the Arrhenius factor, respectively. The constants are provided in Table 5.1.

The Lewis number is set to unity. The model used in OpenFOAM was "unityLewis-Fourier". The Lewis number is a measure of the relative influence of thermal to mass diffusion in different materials [23]. Assuming that the Lewis number is unity is common in combustion studies. A unity Lewis number simplifies the energy conservation equation. Kosasih et al. [21] determined based on the analysis of droplet n-hexane tests that the Lewis number of n-hexane is 1.4943 at room temperature. For a stoichiometric air and n-hexane mixture, this value is for a temperature range of 300 K to 2000 K changes from 2.2 to 2.7[1]. The Lewis number for different hexane-air mixtures as a function of hexane mole fraction is given in Fig. 5.1[2].

A mesh sensitivity analysis was conducted for the Hele-Shaw cell and the one-dimensional ignition simulations presented in Sec. 5.3. The ignition delay time and ignition position

[1] This information was given to me by an internal report of the Explosion Dynamics Laboratory at the California Institute of Technology written by Professor Joseph E. Shepherd

[2] This figure is from an internal report of the Explosion Dynamics Laboratory at the California Institute of Technology written by Professor Joseph E. Shepherd.

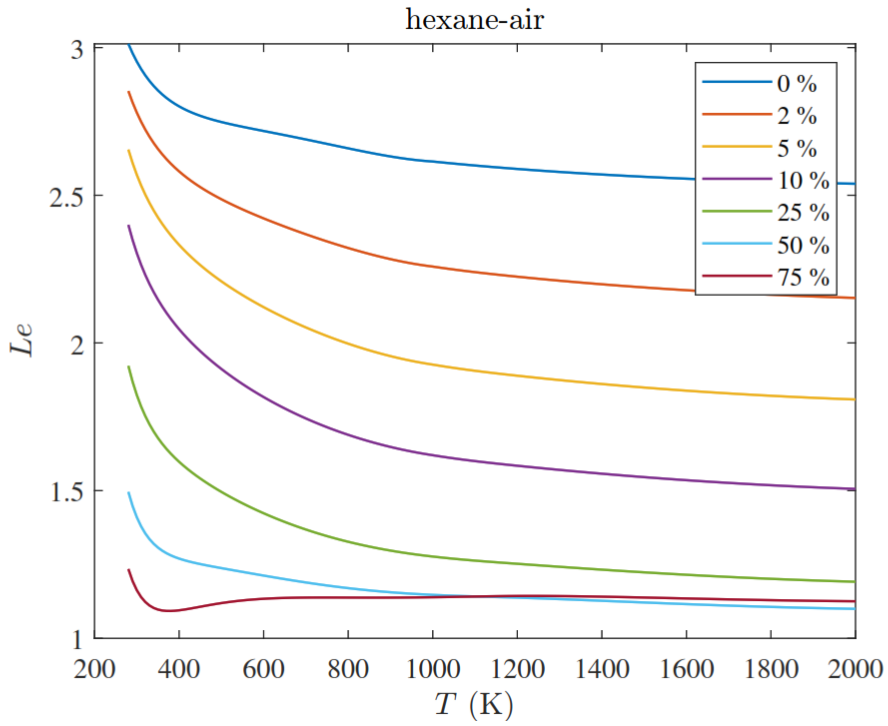


Figure 5.1: Lewis number of hexane in hexane-air mixtures as a function of hexane mole fraction

were used to compare simulations with varying cell sizes, with a threshold of 2 % applied. For the one-dimensional analysis, a uniform cell length of 100 μm was considered in the applied threshold compared to a cell length of 20 μm. For the two-dimensional case, a higher mesh density was applied near the region where ignition is predicted to occur (the top-left quarter of the domain). The rest of the domain was kept the same as described in Sec. 4.3 for the simulations without chemistry, involving only air. A uniform cell length of 167 μm was within the applied threshold compared to a cell length of 70 μm in the same area. From experience, it is recommended to have at least five cells within the thermal boundary layer at the location where ignition occurs, a criterion satisfied by the selected cell size. In Fig. 5.2 a Hele-Shaw cell with the described mesh configuration is illustrated.

5.1 1D Comparison of the `ReactingHeleShawFoam` Solver

This section compares the `ReactingHeleShawFoam` solver to the `buoyantReactingFoam` solver to check for problems in the implementation. Since the velocity is defined differently for the two solvers because of the Hele-Shaw approximations, the gravity was set to zero to eliminate convection. The simulations were implemented as one-dimensional. The comparison is illustrated in Fig. 5.3. As it is visible there is no difference between the results of these two solvers. Nevertheless, this is expected since the `ReactingHeleShawFoam` solver is based on the `buoyantReactingFoam solver`. This is also a valid argument for other temperatures and lengths.

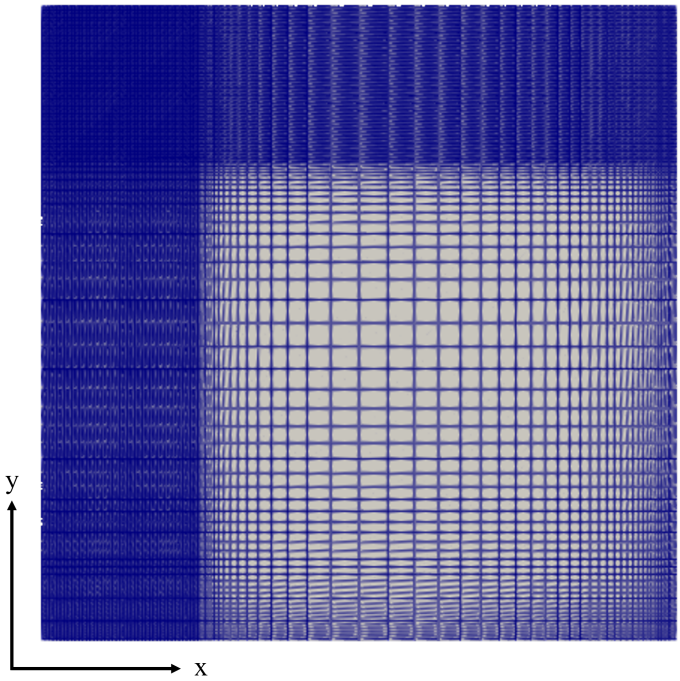


Figure 5.2: Optimal computational domain for a Hele-Shaw cell with dimensions of 0.1 m in both height and length and a gap size of 0.005 m with cell compression near the walls, and a cell size of 167 μm in top-left quarter of the domain

Table 5.1: Constants to model a one-step irreversible stoichiometric air and n-hexane mixture at a pressure of one bar and a temperature of 300 K

Parameter	Value
Molecular Weight of Reactants/Products	30.0913 g mol^{-1}
Activation Temperature (Activation Energy Divided by the General Gas Constant)	17986.576 K
Arrhenius Pre-Exponential Factor A (Eq. 5.1)	0.3 K$^{-2.7}$ s^{-1}
α of the modified Arrhenius rate law (Eq. 5.1)	2.7
Sutherland Coefficient A_s of Reactants/Products (Eq. 4.1)	1.51922487e-6 kg m^{-1} s^{-1} K$^{-1/2}$
Sutherland Coefficient T_s of Reactants/Products (Eq. 4.1)	148.1261 K
Heat Capacity at Constant Pressure (C_p) of Reactants a_1 (Eq. 4.5, C_p is constant)	4.823146 J K^{-1}
Heat Capacity at Constant Pressure (C_p) of Products a_1 (Eq. 4.5, C_p is constant)	4.764285 J K^{-1}
b_1 for Reactants	-2.132861e3 J
b_1 for Products	-1.221446e3 J
b_2 for Reactants/Products	0

The solver was also compared to a detailed multi-species (62 species with 230 reactions)[3] simulation[4] yet again one-dimensional (Fig. 5.4). The multi-species simulation background

[3] https://shepherd.caltech.edu/EDL/PublicResources/sdt/SDToolbox/cti/hexaneReduced.cti

[4] The simulation results were given by Mr. Branson Davis (PhD student at the California Institute of Technology)

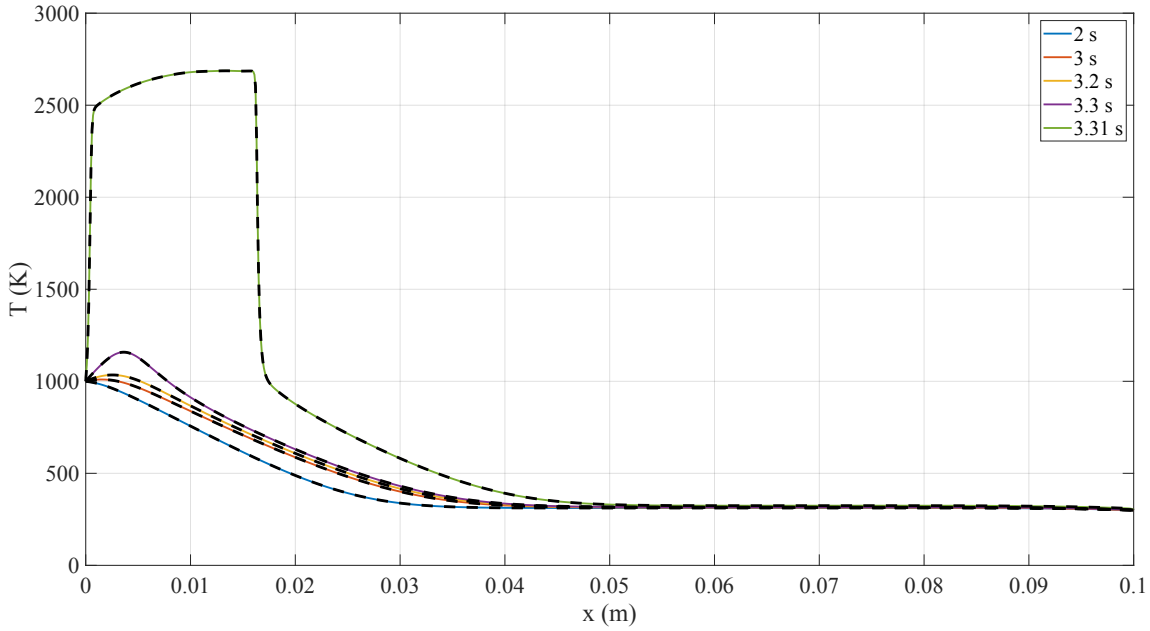


Figure 5.3: Comparison of the `ReactingHeleShawFoam` solver (solid colored lines) to the `buoyantReactingFoam` solver (black dashed lines) for a hot wall temperature of 1000 K, and a cold wall temperature of 300 K

is described by Coronel et al. in [10]. As it is evident, the ignition occurs sooner in the multi-species simulation. This could be because, in the one-step model the contribution of the intermediate species is neglected. The assumption that the Lewis number equals unity could also be the reason for the different ignition times of the two described simulations. The overall structure of the plots shows similarities for the evolution of temperature.

5.2 Zero-Dimensional Adiabatic Ignition Delay Time

To define the zero-dimensional adiabatic reaction limit, which represents the shortest possible ignition delay time with no heat loss, the zero-dimensional adiabatic ignition delay time was calculated with the one-step irreversible chemistry model[5]. The results are illustrated in Fig. 5.5. As described in Sec. 6.3, the ignition temperature in the current study is defined as 1050 K, therefore the zero-dimensional adiabatic ignition delay time is 0.335 seconds.

[5]The code for this calculation was provided to me by Mr. Branson Davis (PhD student at the California Institute of Technology)

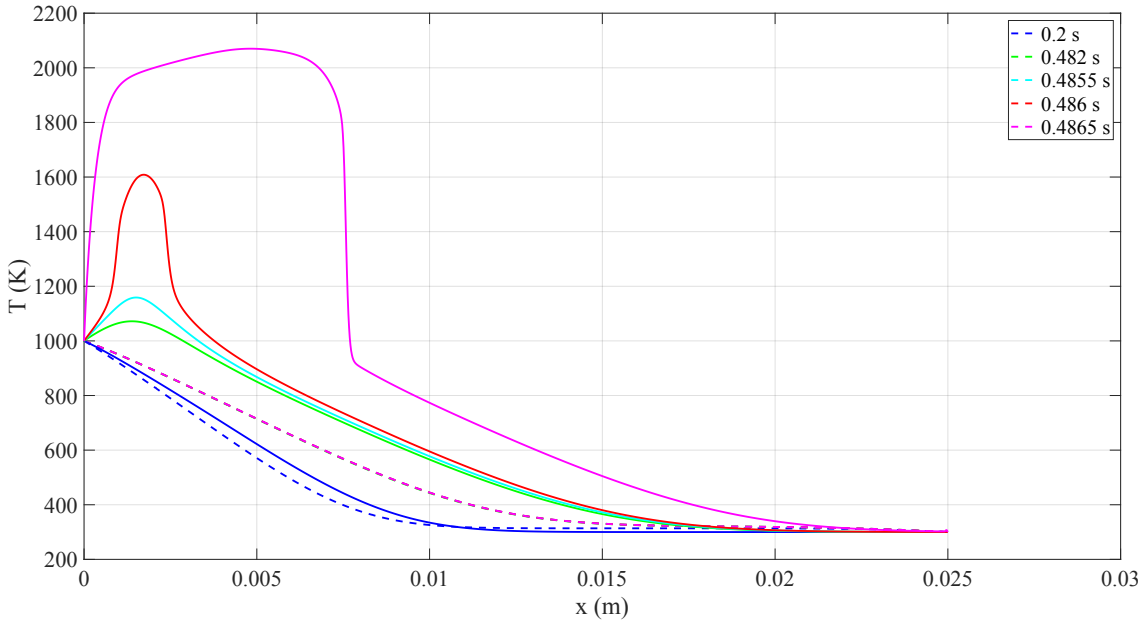


Figure 5.4: Comparison of the `ReactingHeleShawFoam` solver with the one-step reaction (dashed lines) to a high fidelity multi-species reaction simulation (solid lines) for a hot wall temperature of 1000 K, and a cold wall temperature of 300 K

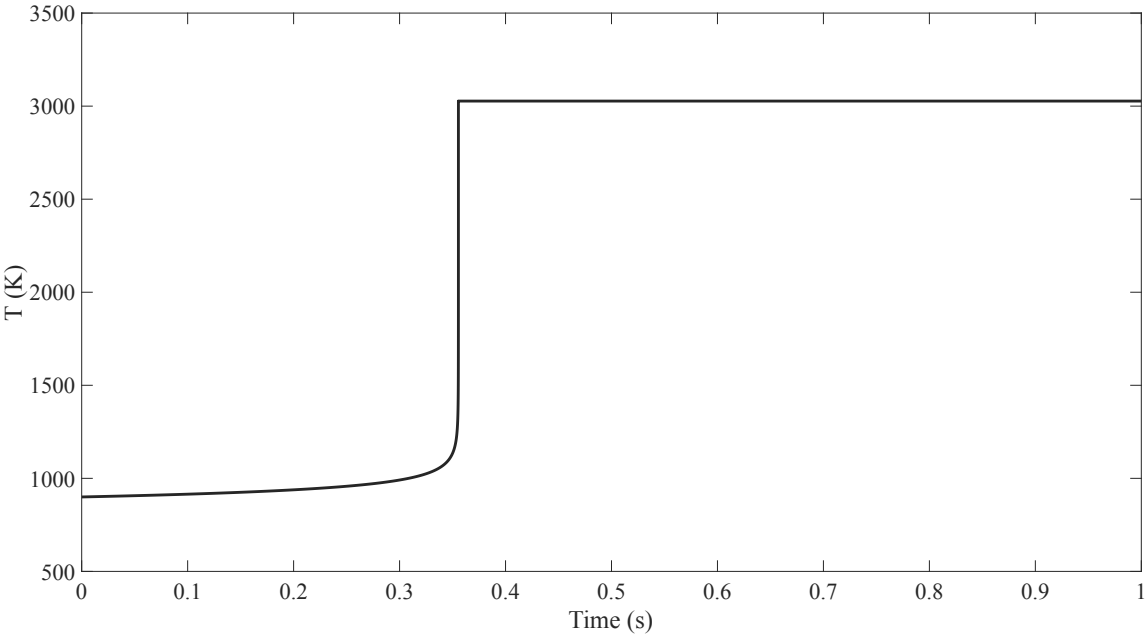


Figure 5.5: Zero-dimensional adiabatic reaction of a stoichiometric air and n-hexane mixture to define the ignition delay time

6 Results and Discussion

This chapter presents the results of the numerical simulations conducted to investigate fluid dynamics and ignition phenomena in thin confined spaces. The findings are organized into three sections: firstly, the validation of the newly implemented solver in OpenFOAM against the Hele-Shaw approximations (Sec. 6.1). Next, the fluid dynamics within Hele-Shaw cells of varying sizes are analyzed in detail (Sec. 6.2). Finally, the ignition behavior of a stoichiometric air and n-hexane mixture under different Hele-Shaw cell sizes is examined (Sec. 6.3).

6.1 Validation of the Developed Solver

Testing the validity of the new solver, as developed and implemented in this study, would be imperative. The challenge is that the existing experimental studies are not numerically reproducible, since creating adiabatic and isothermal boundary conditions is difficult in experimental setups. Furthermore, in the existing works, data are primarily visualization (instantaneous streamlines) of Hele-Shaw flows, but numerical quantities required for validation are not given. In existing numerical studies, the issue is that the provided information is not sufficient to reproduce the reported result. As there is no previous data available that could be used to validate the solver, other means must be sought to examine whether the assumptions and the developed solver are valid.

To test the assumption of a the parabolic velocity profile over the gap, three-dimensional simulations were performed with the `buoyantPimpleFoam` solver (Sec. 6.1.1). An important assumption for the validity of the Hele-Shaw approximations, as implemented in this work, is that the temperature across the gap must remain constant, which was also examoned (Sec. 6.1.2). It has also been demonstrated that three-dimensional simulations with the `buoyantPimpleFoam` solver have comparable results to those of the present solver (Sec. 6.1.3). A Hele-Shaw cell with a length of 0.1 m, a height of 0.3 m, and a gap width of 0.005 m was selected as the reference Hele-Shaw cell with the same boundary conditions as described in Chapter 3. All results in this section are presented after reaching the steady-state solution. Overall, the `Adiabatic_heleShawFoam` solver, which incorporates the Hele-Shaw approximations, has proven to be reliable and quantitatively accurate.

6.1.1 Parabolic Velocity Profile Over the Gap

In Sec. 2.2 it has been presented that the velocity profile over the gap has to be parabolic for the Hele-Shaw approximations to apply. In order to show that this is valid, the velocity profile over the gap from the 3-dimensional simulation has been extracted. After this,

the "Curve Fitter" app in Matlab was used to determine how close the results were to a parabolic function. This has been done for four lines, illustrated in Fig. 6.1.

After fitting the data with the "Curve Fitter" app, the goodness of fit was evaluated with the R^2 (R-Squared) parameter. This statistic measures how successful the fit is in explaining the variation of the data, and is given by the following equation:

$$R^2 = 1 - \frac{\sum_{i=1}^{n}(y_i - \hat{y}_i)^2}{\sum_{i=1}^{n}(y_i - \bar{y})^2} \tag{6.1}$$

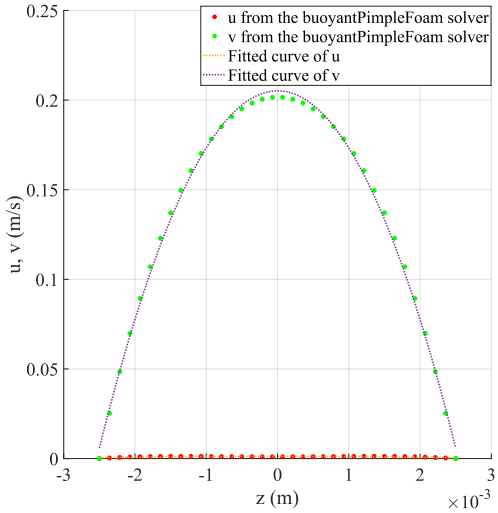
where y_i is the response value, $\hat{y}_i$ is the fit to the response value, and $\bar{y}$ is the overall mean [8]. A value closer to unity indicates that the model has a smaller random error component and also the fit will be more useful for prediction. The calculated R-square parameters are given in Table 6.1. For the line in the z-direction through point D, it is visually obvious that the velocity over the gap is not parabolic. This is though expected, as the velocity close to the corners also has a velocity component in the z-direction. Nonetheless, this is not aligned with the assumption that the velocity in the z-direction is zero in the Hele-Shaw approximations, illustrated in Fig. 6.2. It appears visually and by the given R-squares besides in the corners that there is a nearly perfect parabolic velocity profile. The poor R-square value for u for the line in the z-direction through point A is given by a very low velocity compared to v as it is also visible in Fig. 6.1a. As a result, the poor R-squared value is not important in this case. The results also show that a gap length of 0.005 m is sufficient for the Hele-Shaw approximations within the range of sizes investigated in this study because of the given parabolic velocity profiles.

Table 6.1: SSE values for different points to demonstrate the goodness of fit

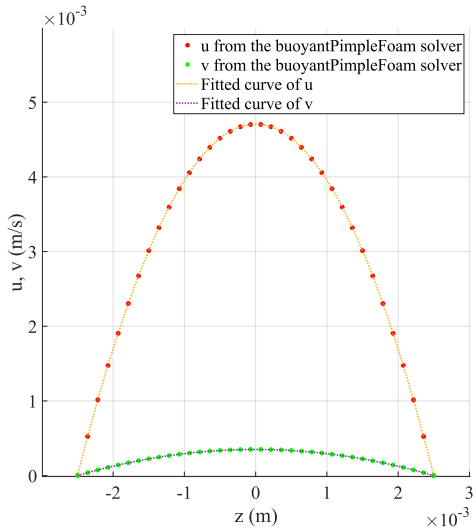
Line	R^2 Value for u	R^2 Value for v
A	0.5556	0.9979
B	1.0000	1.0000
C	1.0000	1.0000
D	0.9514	0.7772

6.1.2 Temperature Profile Over the Gap

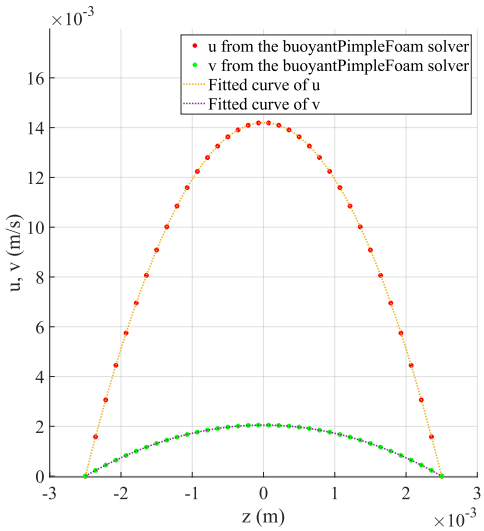
In Sec. 2.2 constant density, temperature, pressure, and mass fraction over the gap are assumed to get the relevant equation set introduced in Sec. 2.3. From the 3-dimensional simulations with the `buoyantPimpleFoamSolver` it was visible that within the simulation precision, the temperature over the gap is constant for most of the domain of the Hele-Shaw cell. This was predictable since there was no mass or thermal diffusion through the adiabatic walls. The pressure over the gap was also constant. Just, where the solver was not performing well in Sec. 6.1.1, also the temperature was not performing well. In Fig. 6.3 the temperatures over the gap are displayed. Furthermore, as the fluid follows the ideal gas law and also the lack of diffusion through the adiabatic walls, it is reasonable to consider that the mass fraction and density are also constant over the gap.



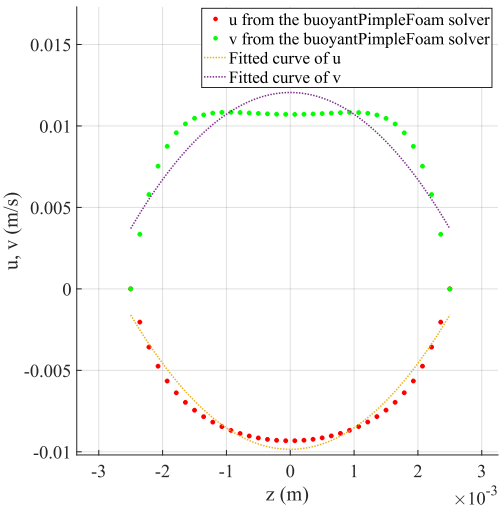
(a) Velocity profile over the line in the z-direction passing through $\underline{x}_A = (0.005, 0.05)$ m



(b) Velocity profile over the line in the z-direction passing through $\underline{x}_B = (0.05, 0.15)$ m



(c) Velocity profile over the line in the z-direction passing through $\underline{x}_C = (0.075, 0.225)$ m



(d) Velocity profile over the line in the z-direction passing through $\underline{x}_D = (0.0005, 0.0005)$ m

Figure 6.1: Parabolic functions fitted to the velocity profiles across the gap of a Hele-Shaw cell with a length of 0.1 m, a height of 0.3 m, and a gap width of 0.005 m after reaching the steady-state solution

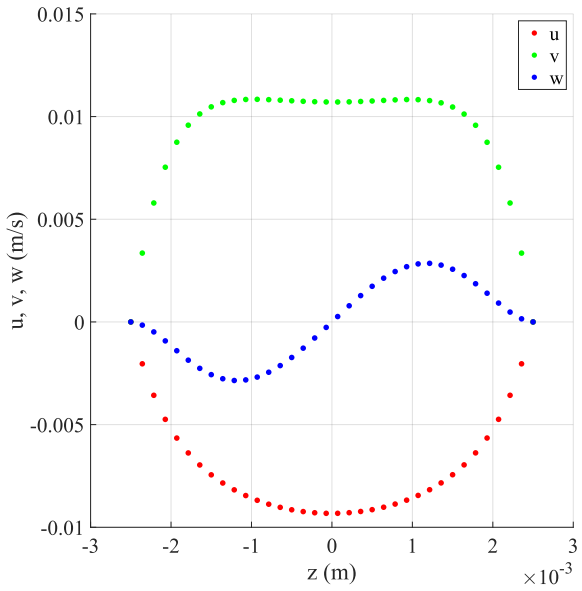


Figure 6.2: Velocity profile over the line in the z-direction passing through $\underline{x}_D = (0.005, 0.005)$ m of a Hele-Shaw cell with a length of 0.1 m, a height of 0.3 m, and a gap width of 0.005 m after reaching the steady-state solution

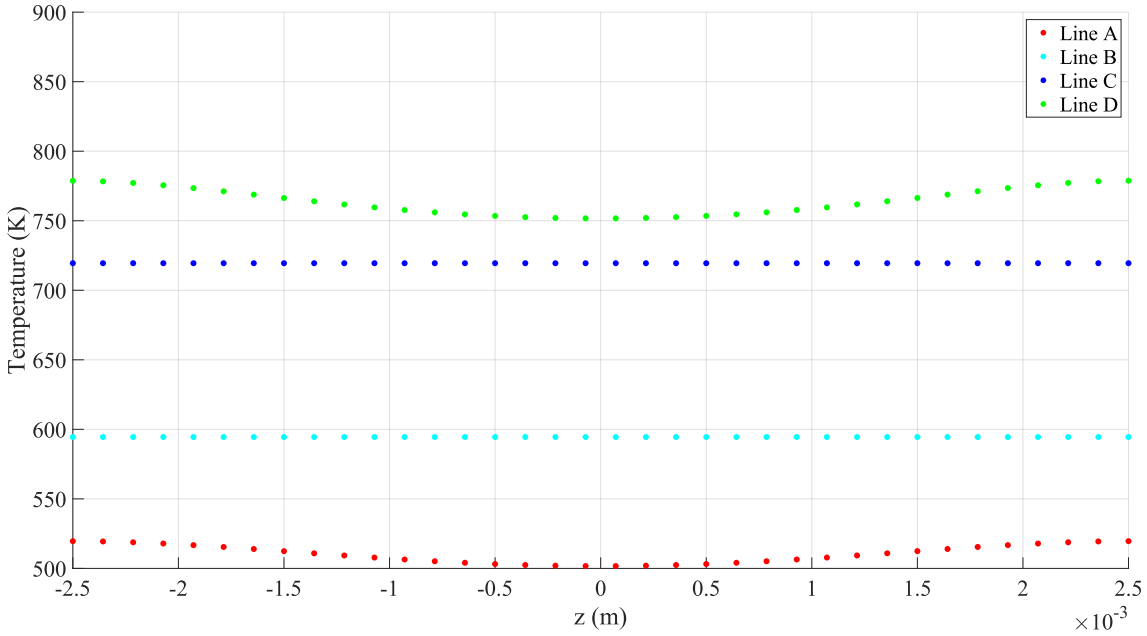


Figure 6.3: Temperature profiles across the gap of a Hele-Shaw cell with a length of 0.1m, a height of 0.3m, and a gap width of 0.005 m after reaching the steady-state solution

6.1.3 Comparison of Two Solvers

6.1.3.1 Local Visual Comparisons

Similar to Sec. 6.1.1 the profiles of the four lines (A-D) were analyzed (displayed in Fig. 6.4). For the `Adiabatic_heleShawFoam` solver, the profile was displayed by the following function:

$$u_{2D}(x,y,z) = \frac{3}{2}u(x,y)\left[1-\left(\frac{2}{b}\right)^2 z^2\right] \tag{6.2}$$

$$v_{2D}(x,y,z) = \frac{3}{2}v(x,y)\left[1-\left(\frac{2}{b}\right)^2 z^2\right] \tag{6.3}$$

It is evident that the `Adiabatic_heleShawFoam` solver predicts higher velocities compared to the 3-dimensional solver. This can be physically explained, as the solver does not account for velocities in the z-direction near the corners. Since there is no significant temperature difference between the two solvers, the higher velocities can be attributed to the conservation of energy.

6.1.3.2 Global Comparison

For a global comparison, a modified L2-error norm was used. In order to show that the newly implemented solver works and that the assumptions are valid the following modified L2-error norm was calculated:

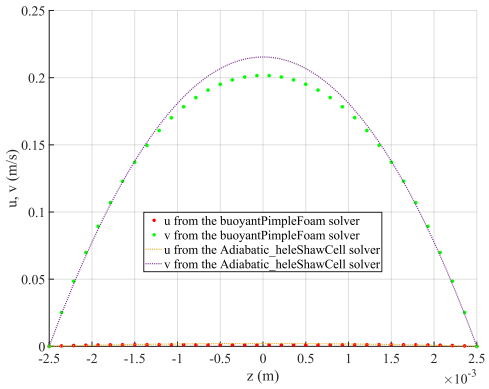
$$L_2 \text{ error norm } := \sqrt{\frac{1}{V}\frac{1}{N}\sum_i^N V_i\left(f_{i,2D} - \langle f_i\rangle_{avg}\right)^2} \tag{6.4}$$

Where f_i is either the temperature, or velocity component in the x and y direction, and $\langle f_i\rangle = \frac{1}{b}\int_{-b/2}^{b/2} f_{i,3D}dz$ of the three-dimensional simulation. V is the volume of the whole domain, and V_i is the volume of a single cell. N is the total number of points calculated by OpenFOAM. $f_{i,2D}$ represents the calculated parameter, respectively, from the simulation using the Hele-Shaw approximations.

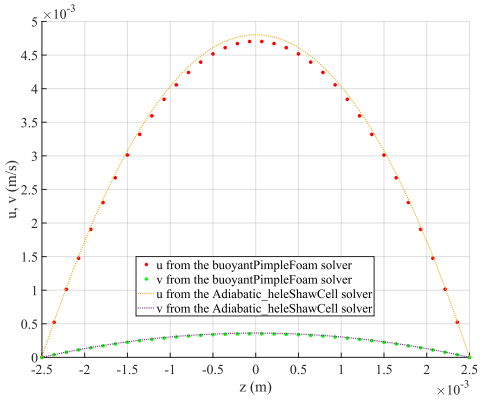
Eqs. 6.4 contains the assumptions made in the new solver with the averaging of the velocity in the z-direction. The modified L2-error norms are a suitable way to quantize the global comparison. However, as there are no other values to compare the results, another approach was used to show the L2-error norm. The second way to modify the L2-error norm is named "L2-relative error norm", which is defined as:

$$L_2 \text{ relative error norm } := \sqrt{\frac{1}{V}\frac{1}{N}\sum_i V_i\left(\frac{f_{i,2D} - \langle f_i\rangle_{avg}}{\langle f_i\rangle_{avg}}\right)^2} \tag{6.5}$$

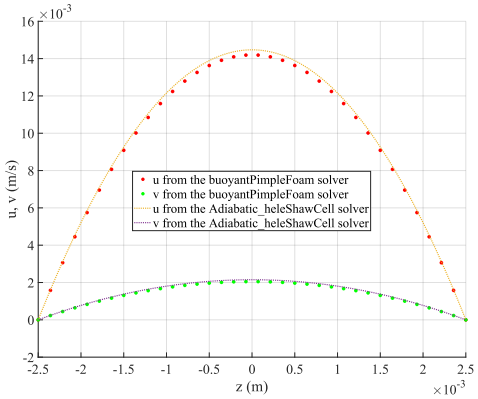
The calculated modified L2-error norms, and L2-relative error norms are given in Table. 6.2. To eliminate interpolation errors, the cell positions of the two simulations in the x- and y-direction are chosen to be the same. The results indicate that the threshold goal of 5 % is satisfied globally.



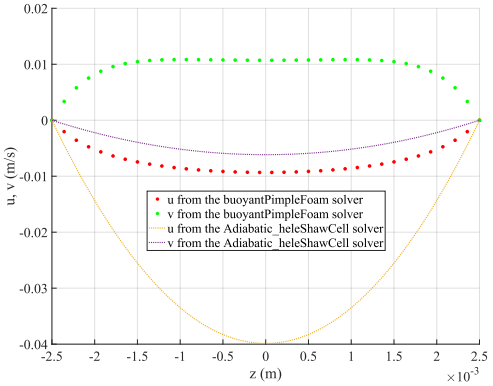
(a) Velocity profile over the line in the z-direction passing through $\underline{x}_A = (0.005, 0.05)$ m



(b) Velocity profile over the line in the z-direction passing through $\underline{x}_B = (0.05, 0.15)$ m



(c) Velocity profile over the line in the z-direction passing through $\underline{x}_C = (0.075, 0.225)$ m



(d) Velocity profile over the line in the z-direction passing through $\underline{x}_D = (0.005, 0.005)$ m

Figure 6.4: Comparison of the `buoyantPimpleFoam` solver (3-D, no approximations) to the `Adiabatic_heleShawFoam` solver (with Hele-Shaw approximations) of a Hele-Shaw cell with a length of 0.1m, a height of 0.3m, and a gap width of 0.005 m after reaching the steady-state solution

Parameter	Modified L2-Error Norm	L2-Relative Error Norm
T	0.056313 K^2	0.0098 %
u	0.000022 $m^2\ s^{-2}$	2.2264 %
v	0.000074 $m^2\ s^{-2}$	2.8919 %

Table 6.2: Values to quantities the global comparison of the `buoyantPimpleFoam` and `Adiabatic_heleShawFoam` solver

6.2 Fluid Dynamics

This section presents the results of the fluid dynamics simulations obtained for Hele-Shaw cells filled with air and varying geometrical configurations (varying length and height). The hot wall temperature (900 K), the cold wall temperature (300 K), the gap length (0.005 m), and the boundary conditions hold the same for all simulations (described in detail in Chapter 3).

For doing so, it was assumed that the gap was infinitely long as it is in Fig. 1.1. The flow was already close or in the transition area to turbulent flow for a confined space with a length and height of 0.1 m and a Rayleigh Number (Ra_L) of 2.542e6 determined with the values given in Table 6.3. The parameters are calculated with Cantera. However, all of the simulations run in this study have a steady solution other than the Hele-Shaw cell with a height of 4.0 m and a length of 0.1 m. The length and height of the simulated cases are all given in Table 6.4.

Table 6.3: Calculated values to determine the Rayleigh number of air at 600 K

Parameter	Value
Thermal diffusivity (κ)	75.4e-6 $m^2\ s^{-1}$
Coefficient of cubical expansion (γ)	1.67e-3 K^{-1}
Kinematic viscosity (ν)	5.129e-5 $m^2\ s^{-1}$

Table 6.4: Simulated cases without chemistry with the `Adiabatic_heleShawFoam` solver for air

	Length	Height		Length	Height		Length	Height
1	0.1 m	0.045 m	9	0.1 m	1.5 m	17	0.2 m	1.0 m
2	0.1 m	0.05 m	10	0.1 m	2.0 m	18	0.3 m	0.1 m
3	0.1 m	0.1 m	11	0.1 m	4.0 m	19	0.3 m	0.3 m
4	0.1 m	0.2 m	12	0.2 m	0.1 m	20	0.4 m	0.1 m
5	0.1 m	0.3 m	13	0.2 m	0.2 m	21	0.5 m	0.1 m
6	0.1 m	0.4 m	14	0.2 m	0.3 m	22	1.0 m	0.1 m
7	0.1 m	0.5 m	15	0.2 m	0.4 m	23	1.5 m	0.1 m
8	0.1 m	1.0 m	16	0.2 m	0.5 m			

The simulation results for a Hele-Shaw cell with dimensions of 0.1 m in length and height are shown in Fig. 6.5, for the system when it has reached steady state conditions. The pressure distribution is nearly uniform across the entire domain. As expected, the temperature gradient near the adiabatic walls is aligned with the surface normals. This behavior is consistent with the adiabatic boundary condition, which prevents heat flux perpendicular to the walls. It is also evident that the thermal boundary layers near the middle of the hot wall are narrower, indicating steeper temperature gradients in these regions. This behavior suggests efficient heat transfer near the hot wall due to the sharp temperature gradients. This is important later to explain physically the position where ignition occurs. Furthermore, in this configuration, the maximum velocity v in the y-direction exceeds the maximum velocity u in the x-direction.

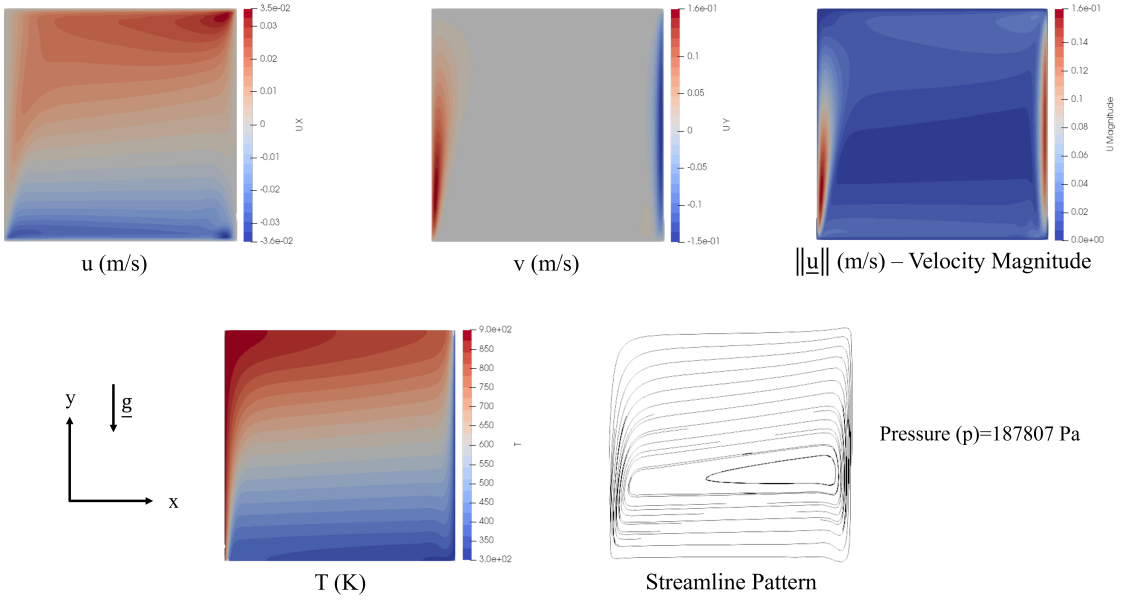


Figure 6.5: Steady-state simulation results for a Hele-Shaw cell with a length and height of 0.1 m

In Fig. 6.6, the simulation results at steady state conditions are shown for two Hele-Shaw cells with dimensions of 0.1 m by 0.3 m and 0.3 m by 0.1 m, respectively. Similar to the previously described configuration, the pressure distribution is nearly uniform across the entire domain. In Fig. 6.7 to Fig. 6.9 the temperature and velocity components are shown along five different horizontal lines located at the bottom, one-quarter of the height, half the height, three-quarters of the height, and the top for a cell with a length and height of 0.1 m and 0.3 m. Similarly, in Fig. 6.10 to Fig. 6.12 the temperature and velocity is displayed for a cell with a length and height of 0.3 m and 0.1 m.

In Fig. 6.6 it is not clearly visible that the boundary condition for the walls is no-slip. However, in Figures 6.8, 6.9, 6.11, and 6.12 the satisfaction of the no-slip condition is observable for all four walls. The velocity at the top and bottom of the cell is zero, which indicates the no-slip condition of the top and bottom walls. The velocity at the beginning and the end of the plots indicates the no-slip boundary condition at the cold and hot walls.

As the temperature at the hot wall gets 900 K for all plots in Fig. 6.7 and Fig. 6.10, and to 300 K at the cold wall the satisfaction of the isothermal walls is also given.

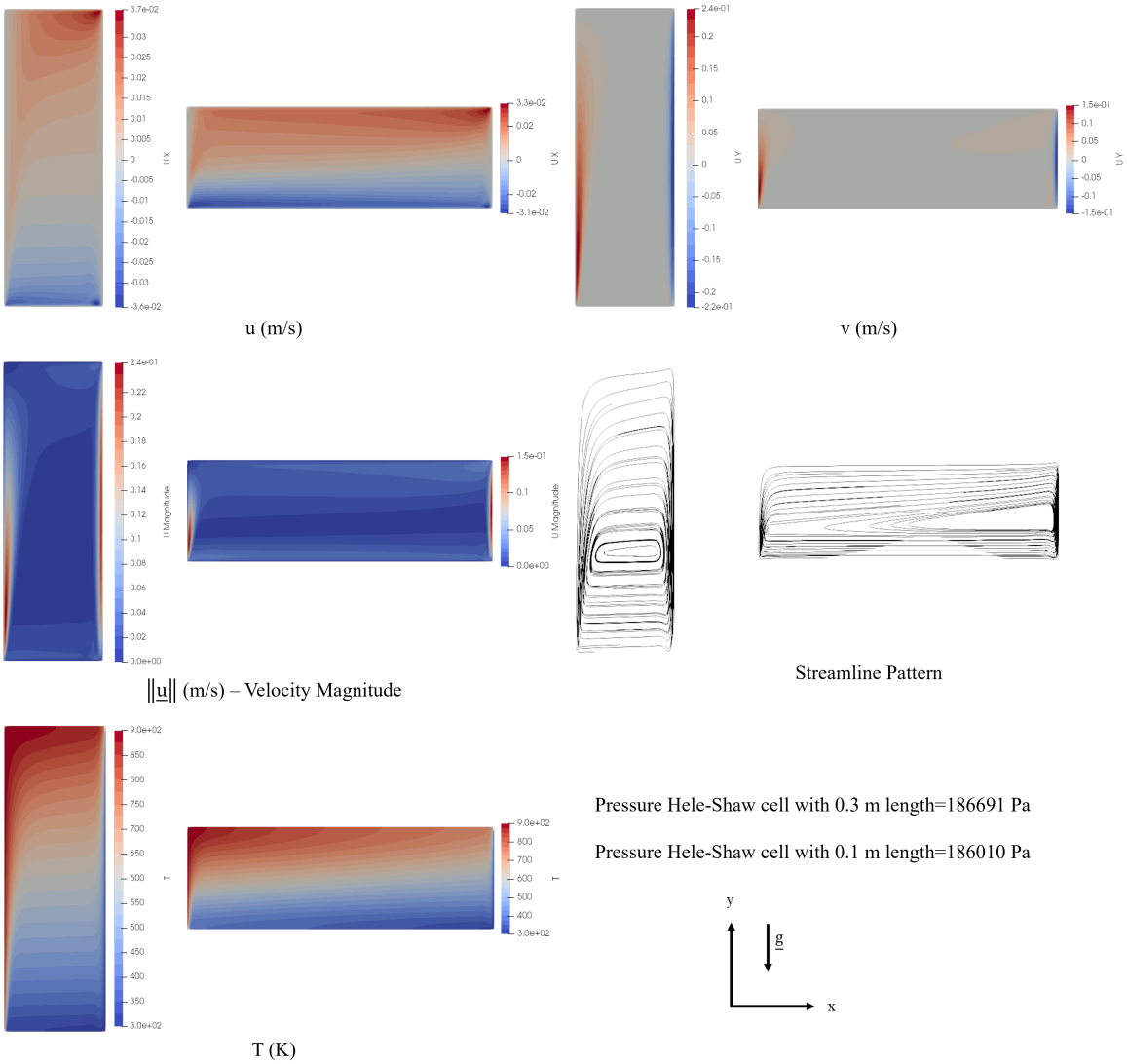


Figure 6.6: Steady-state simulation results for Hele-Shaw cells with a length of 0.1 m and 0.3 m, and a height of 0.3 m and 0.1 m

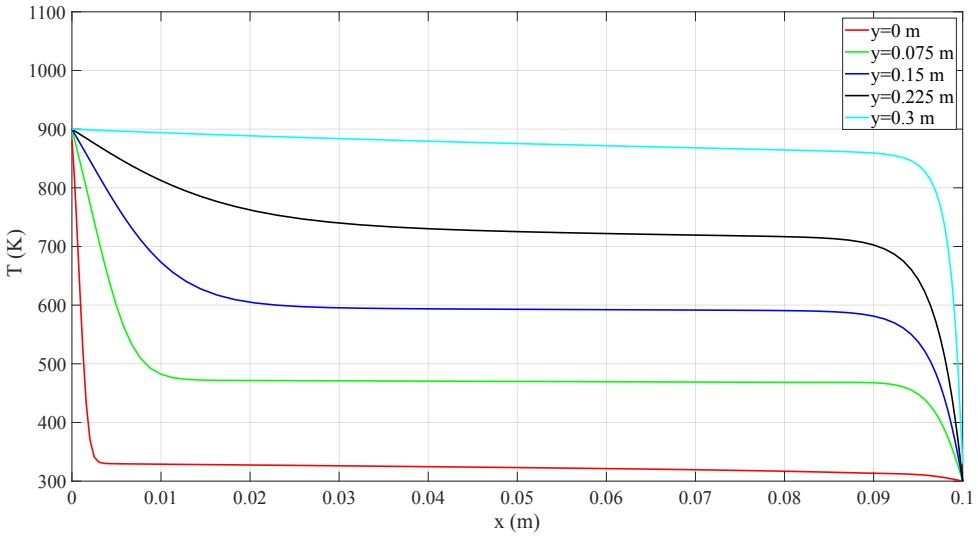


Figure 6.7: Temperature profile over horizontal lines of the steady simulation for the Hele-Shaw cell with a length of 0.1 m and a height of 0.3 m

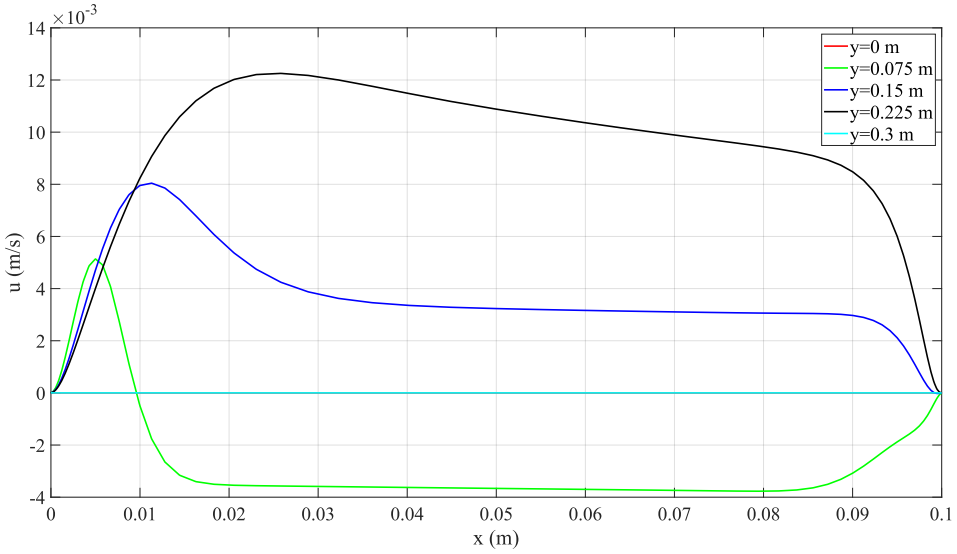


Figure 6.8: Velocity component in the x-direction profile over horizontal lines of the steady simulation for the Hele-Shaw cell with a length of 0.1 m and a height of 0.3 m

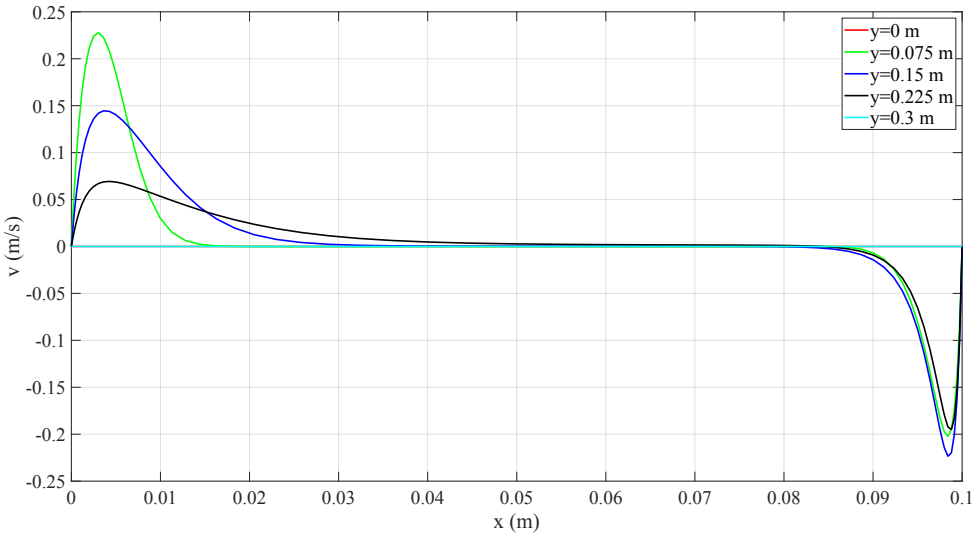


Figure 6.9: Velocity component in the y-direction profile over horizontal lines of the steady simulation for the Hele-Shaw cell with a length of 0.1 m and a height of 0.3 m

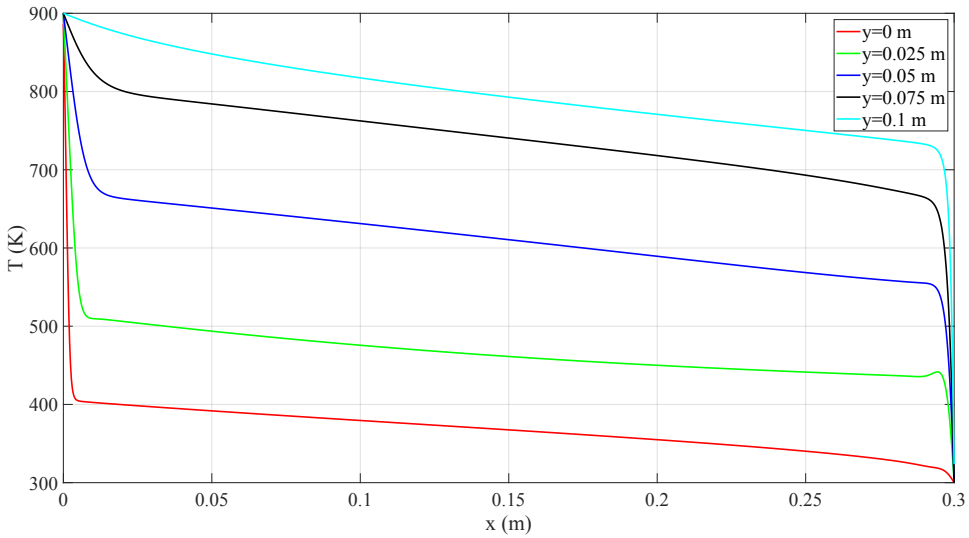


Figure 6.10: Velocity component in the x-direction profile over horizontal lines of the steady simulation for the Hele-Shaw cell with a length of 0.3 m and a height of 0.1 m

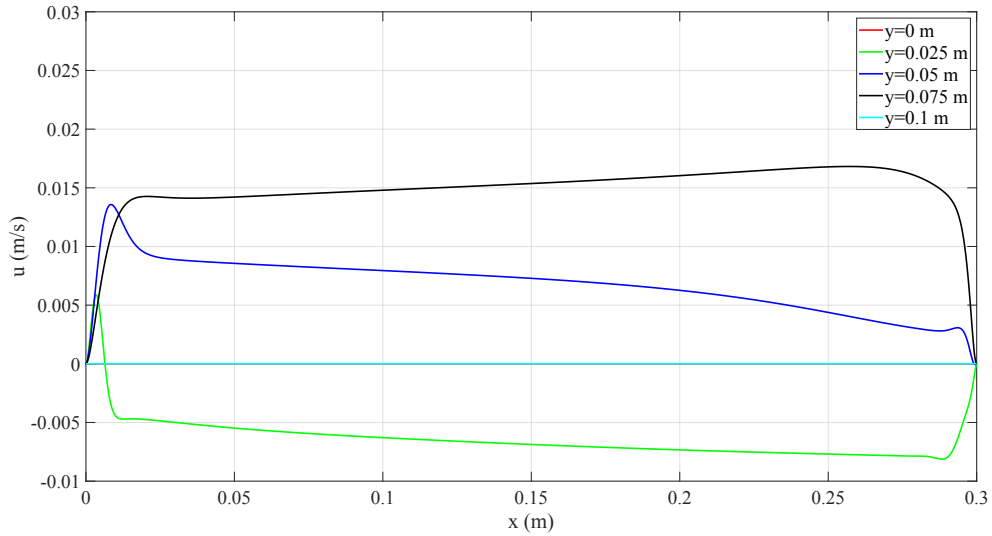


Figure 6.11: Velocity component in the x-direction profile over horizontal lines of the steady simulation for the Hele-Shaw cell with a length of 0.1 m and a height of 0.3 m

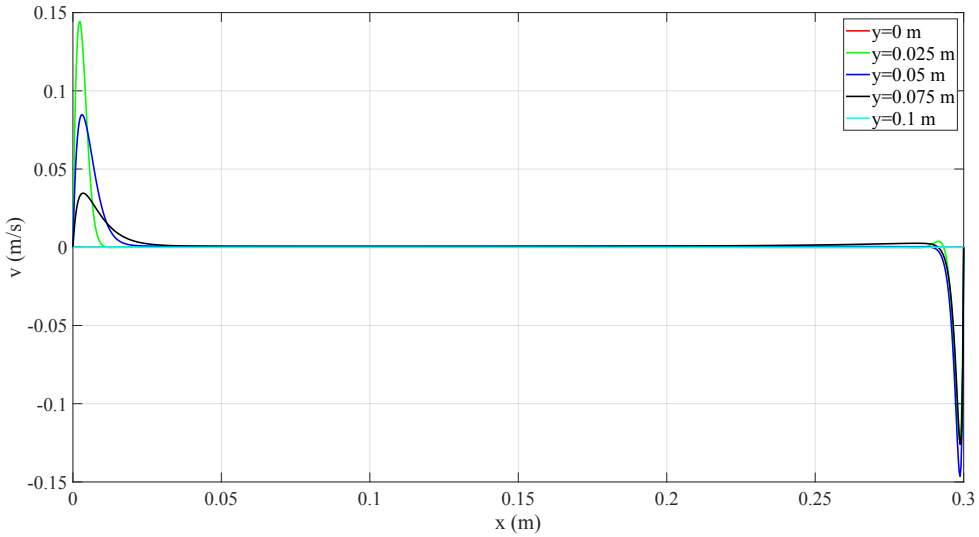
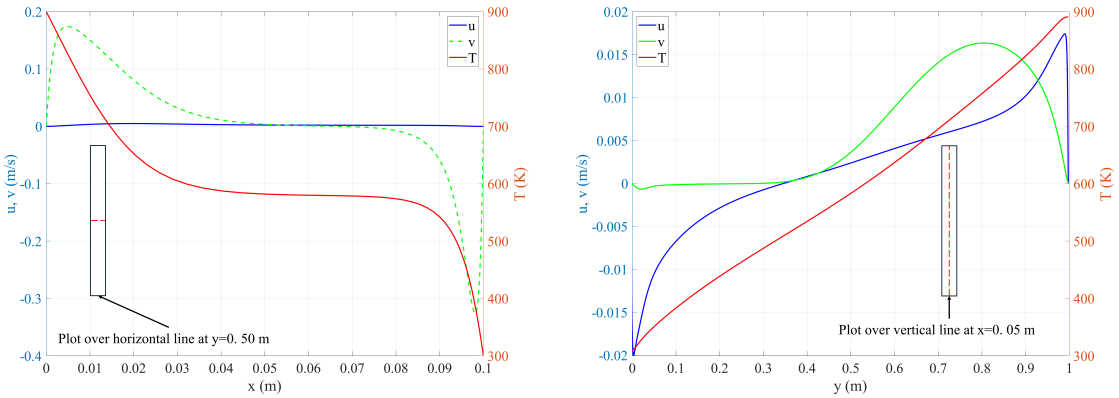


Figure 6.12: Velocity component in the y-direction profile over horizontal lines of the steady simulation for the Hele-Shaw cell with a length of 0.3 m and a height of 0.1 m

To show cases with higher differences between the length and the height, the steady results for the Hele-Shaw cells with dimensions of 0.1 m by 1.0 m and 1.0 m by 0.1 m are shown with plots for better visualization. The plots for the Hele-Shaw cell with 0.1 m length are shown in Fig. 6.13, and for the Hele-Shaw cell with 1.0 m length is shown in Fig. 6.14. The Hele-Shaw cell with a length and height of 0.1 m and 1.0 m shows slightly

more differences in the pressure in a range from 184879 Pa to 184890 Pa due to its longer height compared to the previously discussed Hele-Shaw cells. For the case with a length of 1.0 m, the pressure is 176514 Pa.

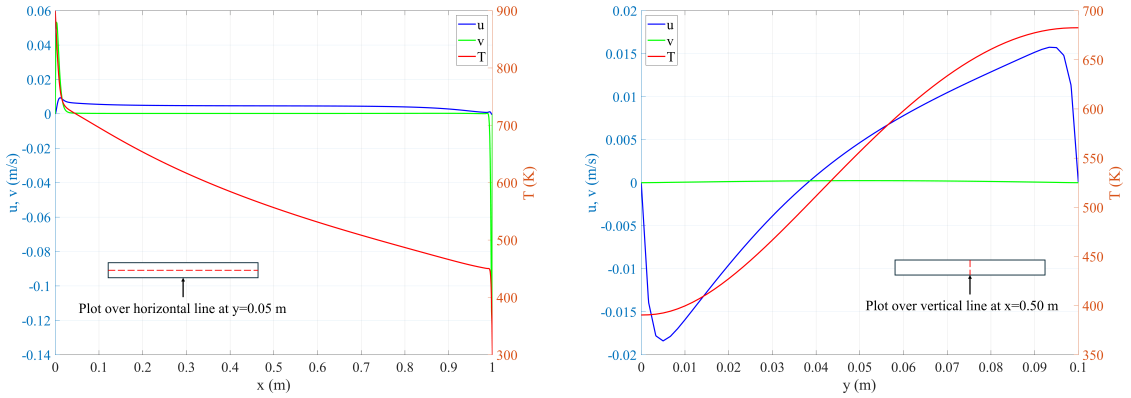
Overall, for all the examined cases, the flow rises along the hot wall and descends along the cold wall. In the center of the domain, the velocity component in the y-direction approaches zero. Since the fluid cannot penetrate the walls, circulation develops within the cell. This circulation causes the flow to be drawn toward the hot wall near the bottom of the domain and pushed toward the cold wall near the top of the Hele-Shaw cell. The temperature gradient is significantly steeper near the hot and cold walls compared to the middle of the domain, where it is more gradual. With the increase in height, the temperature gradient at the hot wall gets smaller, opposing at the cold wall the gradient increases. The thermal boundary layers close to the hot wall are narrow and get thicker towards the cold wall.



(a) Plot over horizontal line at y=0.5 m

(b) Plot over vertical line at x=0.05 m

Figure 6.13: Steady-state simulation results for a Hele-Shaw cell with a length of 0.1 m and a height of 1.0 m. The right vertical axis represents the temperature, while the left vertical axis represents the velocity components.



(a) Plot over horizontal line at y=0.05 m

(b) Plot over vertical line at x=0.5 m

Figure 6.14: Steady-state simulation results for a Hele-Shaw cell with a length of 1.0 m and a height of 0.1 m. The right vertical axis represents the temperature, while the left vertical axis represents the velocity components.

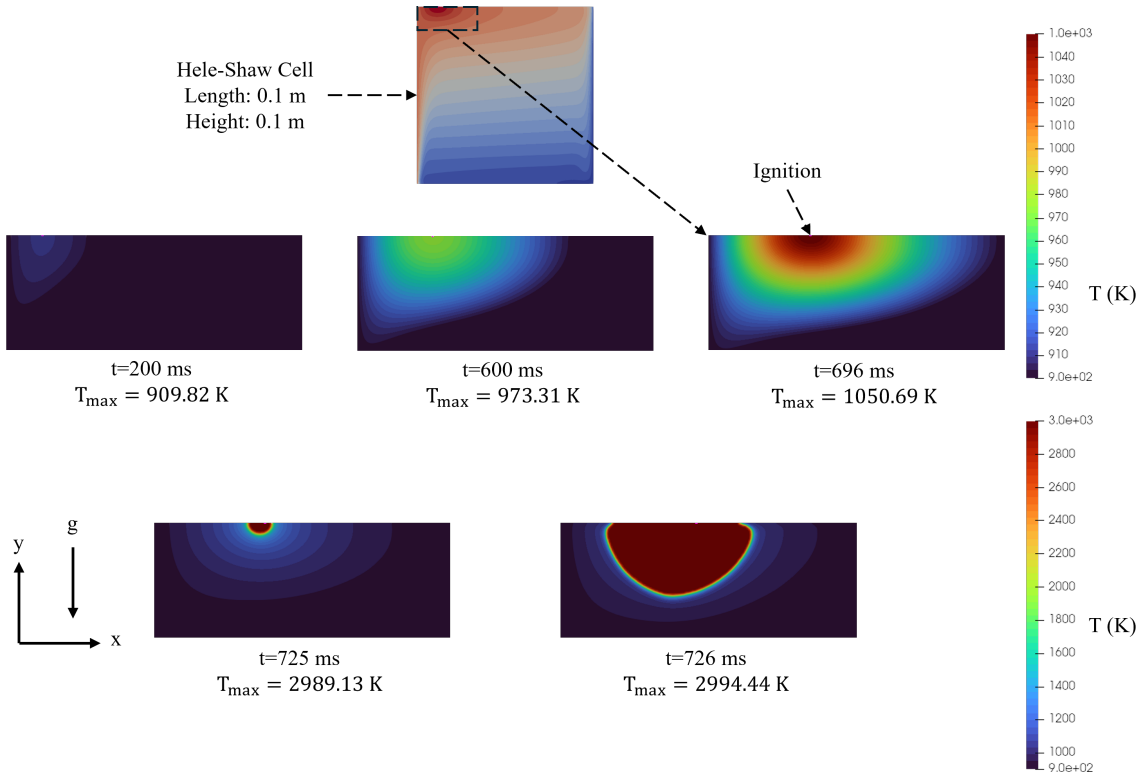
6.3 Ignition Dynamics

This section presents the ignition dynamics results obtained for Hele-Shaw cells filled with a stoichiometric air and n-hexane mixture under varying geometrical configurations (varying length and height). All simulations are initialized from the steady-state solutions of Hele-Shaw cells filled with air and without chemical reactions, as described in Sec. 6.2. The only exception is the unsteady case with a height of 4.0 m and a length of 0.1 m, which will be started after 200 seconds.

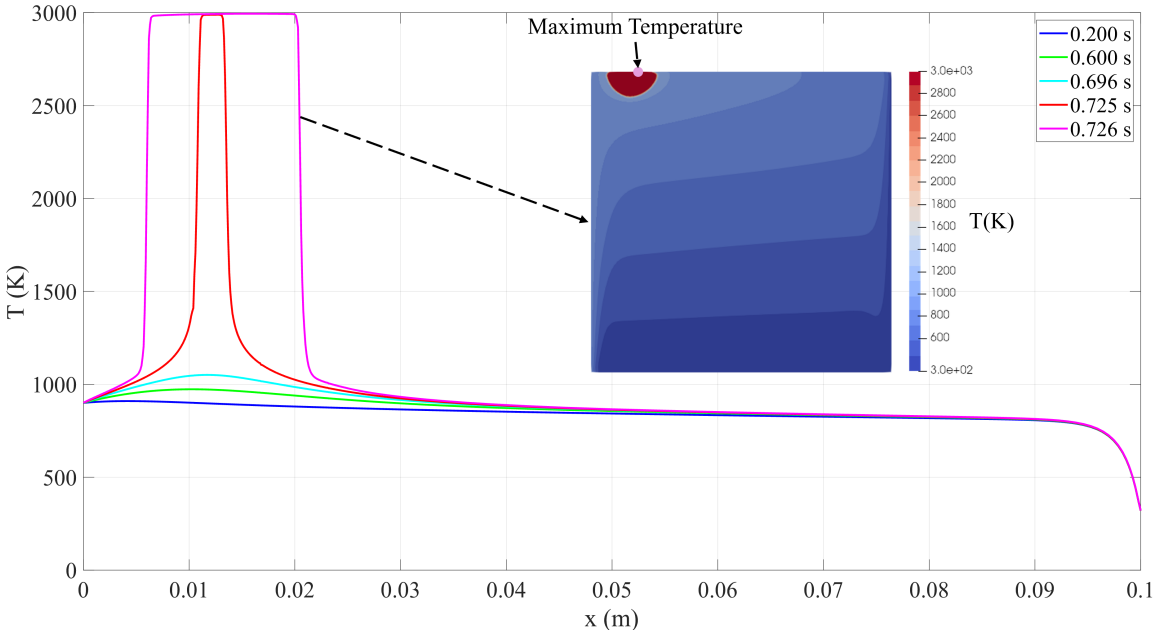
The ignition is determined by the time that the maximum temperature in the domain exceeds 150 K above the peak hot wall temperature. This is used and proposed by other researchers [27, 28, 31]. As a result, in the present study, the ignition is determined when the maximum temperature in the domain gets above 1050 K. The ignition position is determined by the position of the maximum temperature when the domain has reached for the first time step a maximum temperature of 1050 K. All of the simulated cases ignited, besides one case with a height of 0.045 m and a length of 0.1 m.

The igniting Hele-Shaw cell, with a length and height of approximately 0.1 m, is shown in Fig. 6.15a. Ignition occurs at 0.696 seconds. After ignition, a significant temperature rise is observed throughout the domain. The temperature profile over the top wall is shown in Fig. 6.15b.

The ratio of the ignition delay time to the zero-dimensional adiabatic delay time (0.335 seconds, Sec. 5.2) for Hele-Shaw cells with a constant length of 0.1 m and varying height is illustrated in Fig. 6.16, and for a constant height of 0.1 m and varying length is illustrated in Fig. 6.17. The subcritical limit in Fig. 6.16 has to be between the non-igniting case with a height of 0.045 m and the igniting case with a height of 0.05 m. The displayed limit is drawn at a height of 0.0475 m. The subcritical or nonexplosive limit shows the limit to which an ignition event does not occur. Since no losses are considered in the zero-dimensional adiabatic reaction time, the ignition delay time of the Hele-Shaw cells



(a) 2D contour map of the temperature illustrating the ignition kernel and the initial flame propagation



(b) Temperature profiles along the top wall (horizontal line over $y = 0.1$ m) at different time steps

Figure 6.15: Ignition kernel and the initial flame propagation of a Hele-Shaw cell with a length and height of 0.1 m

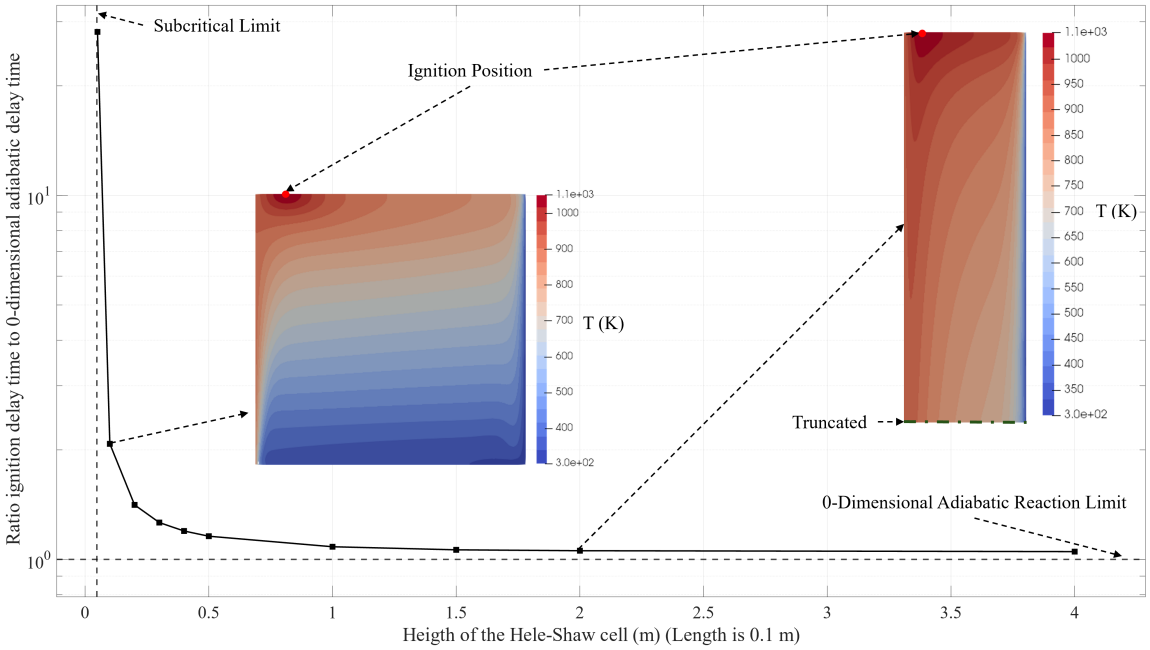


Figure 6.16: Ignition delay times as a function of the varying height of the Hele-Shaw cell with constant lengths of 0.1 m

cannot be less than 0.335 seconds. This can be seen in Fig. 6.16 as the ignition delay times are not getting below the zero-dimensional adiabatic reaction limit.

It is apparent that the ignition delay time decreases as the height or the length increases. This means that with the increase of the surface area, the heat losses decrease. This finding was predictable because, in smaller surface areas of Hele-Shaw cells, convection occurs within a more confined space. As a result, the thermal boundary layers are closer together, leading to increased heat losses. In Fig. 6.18a all of the simulated reaction cases are displayed against the surface area, and in Fig. 6.18b against the aspect ratio (length divided by height). The legend in the Figures shows the parameter that is held constant. The ignition time as a function of the aspect ratio does not exhibit a clear trend, indicating that the aspect ratio is not an appropriate dimensionless parameter for this analysis. The surface area proves to be a more suitable parameter, as it exhibits a clear trend. However, it is not a dimensionless parameter.

In all cases, the ignition occurred on the top adiabatic wall. The position in the x-direction of the cases with a constant height of 0.1 m, and varying lengths occurred around 0.011 m to 0.012 m. For the case with a length of 0.1 m and a varying height, the ignition occurred around 0.011 m and 0.018 m.

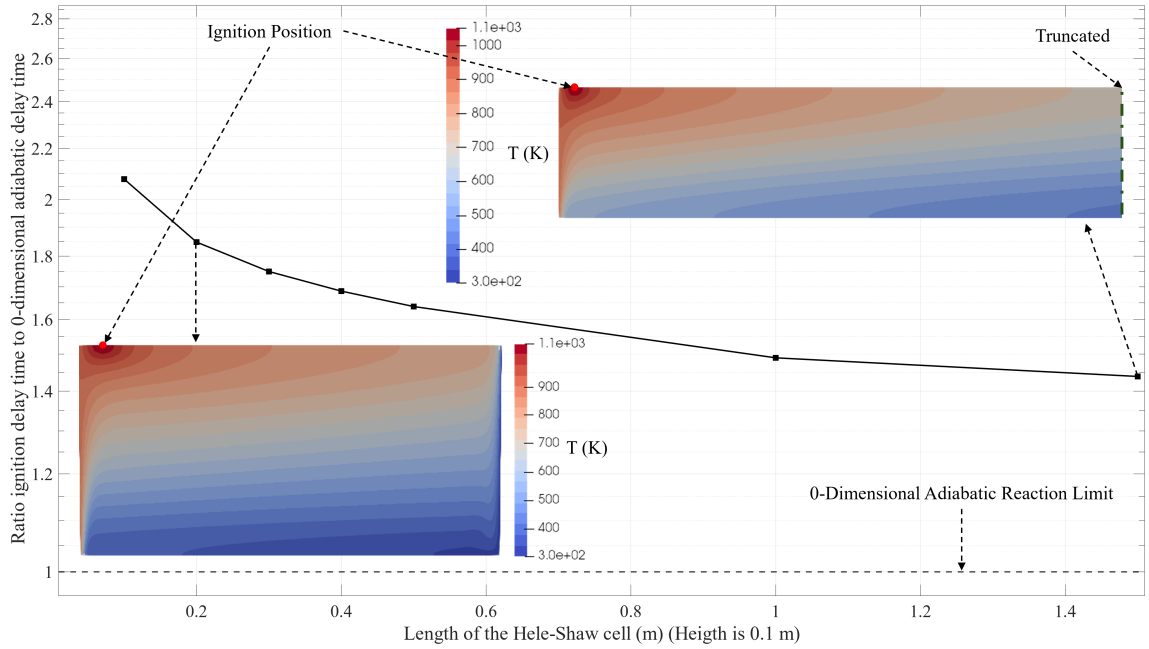
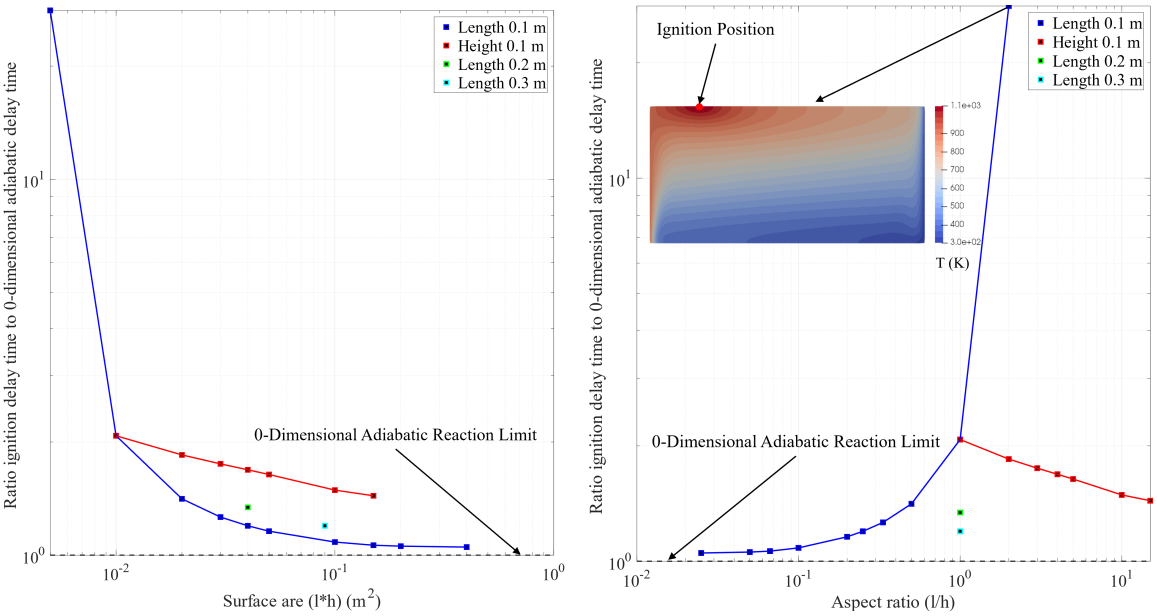


Figure 6.17: Ignition delay times as a function of the varying length of the Hele_Shaw cell with constant heights of 0.1 m



(a) Plot over horizontal line at y=0.5 m

(b) Plot over vertical line at x=0.05 m

Figure 6.18: Steady-state simulation results for a Hele-Shaw cell with a length of 0.1 m and a height of 1.0 m. The right vertical axis represents the temperature, while the left vertical axis represents the velocity components.

7 Conclusions

The goal of this work was to expand the understanding of thermal ignition problems in thin confined spaces, specifically in Hele-Shaw cells, through numerical simulations. First, a new solver with the Hele-Shaw approximations was implemented in OpenFOAM to reduce the problem to two dimensions. A parabolic velocity profile over the narrow gap which is part of the Hele-Shaw approximations was proven mathematically, and in more detail numerically with three-dimensional simulations. Later, the results of the three-dimensional simulation were compared, both globally and locally, to those of the newly implemented solver with the approximations. This also facilitated a better understanding of how well the approximations hold. Overall, the results were satisfactory, with the only exception being the corners, where the approximations are either invalid or less accurate than in the rest of the domain. Based on the previous literature, the used model was also extended to reacting cases for the first time.

After validating the newly implemented solver, the fluid dynamics in Hele-Shaw cells were studied with air for various heights and lengths. As expected, convection caused circulation within the domain. The fluid near the left hot wall rose due to higher temperatures, leading to lower densities, while near the right cold wall, the fluid sank due to lower temperatures and higher densities. In all simulated cases, a single circulation pattern was observed. The thermal boundary layers near the hot wall were thinner compared to the rest of the domain, indicating greater heat loss toward the hot wall relative to other regions.

The results of the fluid dynamics simulations with just air were then used to simulate thermal ignition with a stoichiometric air and n-hexane mixture. The simulations incorporating a chemistry model to capture ignition events were initiated using the initial conditions from simulations conducted with only air and no chemistry model. All simulated cases ignited, besides the Hele-Shaw cell with a length and height of 0.1 m and 0.045 m. A subcritical limit was found for Hele-Shaw cells with a constant length of 0.1 m. The subcritical limit has to be between a height of 0.045 m and 0.05 m. The zero-dimensional adiabatic reaction ignition delay time was calculated (0.335 s) to find the zero-dimensional adiabatic reaction limit, which the ignition delay time of the Hele-Shaw cells cannot be below this value. This was given in the simulation results. It turned out that as the surface area increases the ignition delay time decreases. This can be attributed to smaller Hele-Shaw cells which experience greater heat loss. Consequently, the ignition delay time is longer, which can be interpreted using simple ignition models such as the Semenov model for thermal ignition. The position where ignition occurred for all simulated cases was at the top adiabatic wall close to the left hot isothermal wall. This could be related to the fact that the heat loss in this area is smaller compared to the rest of the domain, which has similarly high temperatures at the same time.

In general, it can be stated that the topic of ignition in thin confined spaces is an ongoing area of research. Numerical simulations like this are valuable for gaining a better understanding of the physics occurring in Hele-Shaw cells, which is important for industrial safety.

In summary the following observations were made:

- The Hele-Shaw approximations, which assume a parabolic velocity profile over the narrow gap and involve the resulting averaging of the equations, are generally valid for the length scales presented in this study.
- The newly implemented solver showed good agreement with computationally expensive three-dimensional simulations for a reference Hele-Shaw cell, particularly with respect to temperature, which was matched well.
- The simulations of fluid dynamics with air and without a chemistry model can give information to predict where ignition occurs.
- The thermal boundary layers close to the left hot wall were narrow compared to the rest of the domain, which leads to higher heat losses in this area.
- All simulated cases ignited at the top adiabatic wall.
- The ignition delay time decreases as the size of the Hele-Shaw cells increases.

7.1 Future Work

In the current study besides the left and right isothermal walls, the other walls were assumed to be adiabatic. However, recreating such a Hele-Shaw cell in laboratories is challenging. Therefore, an extension of the model to walls with heat flux (non-adiabatic) instead of the adiabatic walls helps to do also experimental work on thermal ignition in thin confined spaces to gain a better understanding of such circumstances.

Investigating Hele-Shaw cells heated from below is also an ongoing gap in this field. Accordingly, more accurate simulations be conducted using a more realistic chemistry model, rather than the irreversible one-step chemistry model used in the current study. Another important consideration is to identify a non-dimensional number to characterize the geometry of Hele-Shaw cells, or more generally, confined spaces[1]. This helps to compare different thermal ignition studies more accurately.

[1]At the Explosion Dynamics Laboratories of the California Institute of Technology, Mr. Branson Davis and Mr. Donner Schoeffler are working on this problem.

Bibliography

[1] David J Acheson. *Elementary fluid dynamics*. Oxford University Press, 1990.

[2] ASTM-E659. *Standard test method for autoignition temperature of liquid chemicals*. American Society for Testing and Materials, 2005.

[3] GK Batchelor. "Heat transfer by free convection across a closed cavity between vertical boundaries at different temperatures". In: *Quarterly of Applied Mathematics* 12.3 (1954), pp. 209–233.

[4] Theodore L Bergman et al. *Introduction to heat transfer*. John Wiley & Sons, 2011.

[5] PA Boettcher et al. "The effect of heating rates on low temperature hexane air combustion". In: *Fuel* 96 (2012), pp. 392–403.

[6] Michael Burns et al. "Evaluation of fuel tank flammability and the FAA inerting system on the NASA 747 SCA". In: *US Department of Transportation, Federal Aviation Administration, Office of Aviation Research: Washington, DC, USA* (2004).

[7] Ivan Catton. "Natural convection in enclosures". In: *International Heat Transfer Conference Digital Library*. Begel House Inc. 1978.

[8] "Coefficient of Determination". In: *The Concise Encyclopedia of Statistics*. New York, NY: Springer New York, 2008, pp. 88–91. ISBN: 978-0-387-32833-1. DOI: 10.1007/978-0-387-32833-1_62. URL: https://doi.org/10.1007/978-0-387-32833-1_62.

[9] Jeff D. Colwell, Thomas M. Korb, and Robert E. Peck. "Hot Surface Ignition of Jet-A Fuel by Conductive Deposits". In: *Proceedings of the Combustion Institute* 29.1 (Jan. 2002), pp. 297–303. (Visited on 10/03/2021).

[10] S Coronel et al. "Reduction methodology for detailed kinetic mechanisms: application to n-hexane-air hot surface ignition". In: *Asia Pacific Combustion Conference*. Vol. 11. 2017.

[11] Branson Davis, Charline Fouchier, and Joseph Shepherd. "Fluid Motion and Heat Transfer in Autoignition Testing". 15th International Symposium on Hazards, Prevention and Mitigation of Industrial Explosions, Naples, ITALY June 10-14, 2024. 2024.

[12] JW Elder. "Laminar free convection in a vertical slot". In: *Journal of Fluid Mechanics* 23.1 (1965), pp. 77–98.

[13] JW Elder. "Numerical experiments with free convection in a vertical slot". In: *Journal of Fluid Mechanics* 24.4 (1966), pp. 823–843.

[14] JW Elder. "Turbulent free convection in a vertical slot". In: *Journal of fluid mechanics* 23.1 (1965), pp. 99–111.

[15] Charline Fouchier and Joseph Shepherd. "ASTM E659 Standardized Test Analysis and Results for Synthetic Paraffinic Kerosene". 15th International Symposium on Hazards, Prevention and Mitigation of Industrial Explosions, Naples, ITALY June 10-14, 2024. 2024.

[16] David G. Goodwin et al. *Cantera: An Object-oriented Software Toolkit for Chemical Kinetics, Thermodynamics, and Transport Processes*. `https://www.cantera.org`. Version 3.0.0. 2023. DOI: `10.5281/zenodo.8137090`.

[17] C Günther and U Müller. *Rayleigh-Benard Convection in a Hele-Shaw eil*. Tech. rep. KFK 4212. Kernforschungszentrum Karlsruhe, 1987.

[18] Beverly K Hartline and CRB Lister. "Thermal convection in a Hele-Shaw cell". In: *Journal of Fluid Mechanics* 79.2 (1977), pp. 379–389.

[19] Andreas Heintz. *Thermodynamik der Mischungen: Mischphasen, Grenzflächen, Reaktionen, Elektrochemie, äußere Kraftfelder*. Springer-Verlag, 2017.

[20] Colson Johnson and Chad V Mashuga. "Characterizing the autoignition behavior of simple paraffins and alcohols; comparisons and implications". In: *Journal of Loss Prevention in the Process Industries* 77 (2022), p. 104773.

[21] Engkos Achmad Kosasih et al. "Heat and mass transfer droplets of n-Hexane and n-Heptane towards temperature and rate of air flow rate variations". In: *AIP Conference Proceedings*. Vol. 2062. 1. AIP Publishing. 2019.

[22] JM Kuchta, A Bartkowiak, and MG Zabetakis. "Hot Surface Ignition Temperatures of Hydrocarbon Fuel Vapor-Air Mixtures". In: *Journal of Chemical and Engineering Data* 10 (1965), pp. 282–288.

[23] Chung K Law. *Combustion physics*. Cambridge University Press, 2010.

[24] RK MacGregor and Ashley Francis Emery. "Free convection through vertical plane layers—moderate and high Prandtl number fluids". In: *Journal of Heat Transfer* 91.3 (1969), pp. 391–401.

[25] Conor Daniel Martin. "Experiments in Thermal Ignition: Influence of Natural Convection on Properties of Gaseous Explosions". PhD thesis. California Institute of Technology, 2023.

[26] Bonnie J McBride. *Coefficients for calculating thermodynamic and transport properties of individual species*. Vol. 4513. NASA Langley Research Center, 1993.

[27] J Melguizo-Gavilanes et al. "Hot surface ignition of stoichiometric hydrogen-air mixtures". In: *international journal of hydrogen energy* 42.11 (2017), pp. 7393–7403.

[28] Josué Melguizo-Gavilanes et al. "Hot surface ignition of n-hexane mixtures using simplified kinetics". In: *Combustion Science and Technology* 188.11-12 (2016), pp. 2060–2076.

[29] Günter P Merker and Günter P Merker. "Freie Konvektion in Behältern". In: *Konvektive Wärmeübertragung* (1987), pp. 336–381.

[30] Bernard J Scheiner et al. *Investigation of fire and explosion accidents in the chemical, mining, and fuel-related industries: a manual*. Tech. rep. 678-688. 1985.

[31] Donner T Schoeffler and Joseph E Shepherd. “Thermal Ignition by Millimeter-Scale Surface Hot Spots”. 29th International Colloquium on Dynamics of Explosions and Reactive Systems (ICDERS), Siheung, South Korea, July 23-28. 2023.

[32] Joe Shepherd. “Learning from a tragedy: explosions and Flight 800”. In: *Engineering and Science* 61.2 (1998), pp. 18–29.

[33] The Open Foam Foundation. *OpenFOAM*. `https://www.openfoam.org/`. 2023.

[34] David J Tritton. *Physical fluid dynamics*. Springer Science & Business Media, 2012.

[35] SS Vorontsov et al. “Natural convection in a Hele-Shaw cell”. In: *International journal of heat and mass transfer* 34.3 (1991), pp. 703–709.

[36] J Warnatz. “Chemistry of Stationary and Non-Stationary Combustion”. In: *Modelling of Chemical Reaction Systems: Proceedings of an International Workshop, Heidelberg, Fed. Rep. of Germany, September 1–5, 1980*. Springer. 1981, pp. 162–188.

[37] Jurgen Warnatz et al. *Combustion*. Springer, 2006.